A MULTIWAVELENGTH STUDY OF GALACTIC H II REGION Sh 2-294

M. R. Samal,[1] A. K. Pandey,[2,3,1] D. K. Ojha,[3] S. K. Ghosh,[3] V. K. Kulkarni,[4] and B. C. Bhatt[5]
manash@aries.ernet.in, ojha@tifr.res.in

ABSTRACT

We present the observational results of Galactic H II region Sh 2-294, using optical photometry, narrowband imaging, and radio continuum mapping at 1280 MHz, together with archival data from the 2MASS, *MSX*, and *IRAS* surveys. The stellar surface density profile indicates that the radius of the cluster associated with the Sh 2-294 region is $\sim 2.3'$. We estimate the minimum reddening $E(B - V) = 1.35$ mag and a distance of 4.8 ± 0.2 kpc to the region. The ratio of the total to the selective extinction (R_V) is found to be 3.8 ± 0.1, indicates an anomalous reddening law for the dust inside the cluster region. We identified the ionizing source of the H II region, and spectral type estimates are consistent with a star of spectral type $\sim$B0 V. The 2MASS JHK_s images reveal a partially embedded cluster associated with the ionizing source along with a small cluster towards the eastern border of Sh 2-294. The radio continuum and Hα images show the ionization front along the direction of the small cluster. An arc-shaped diffuse molecular hydrogen emission and a half-ring of dust emission are also seen in the direction of the ionization front at 2.12 and 8 μm (*MSX*), respectively. Self-consistent radiative transfer model of mid- to far-infrared continuum emission detected near small cluster is in good agreement with the observed spectral energy distribution of a B1.5 ZAMS star. The morphological correlation between the ionized and molecular gas, along with probable timescale involved between the ionizing star, evolution of H II region, and small cluster, indicates that the star formation activity observed at the border is probably triggered by the expansion of H II region.

Subject headings: dust, extinction — galaxies: star clusters — H II regions — infrared: ISM — ISM: individual (S294) — radio continuum: ISM — stars: formation

Online material: color figures

1. INTRODUCTION

Massive OB star formation takes place in the dense core of molecular clouds and is associated with dense stellar clusters. Their pre–main-sequence (PMS) life scales are much shorter than those of low-mass stars. The stellar winds and radiation emitted from these stars eventually disrupt the molecular cloud, dissociate and ionize the gas, and form the H II regions. The radiation from such stars can modify the interstellar grains present in their immediate vicinity, and hence affect the interstellar extinction law (see Chini & Wargau 1990; Pandey et al. 2000). Thus, change in the interstellar extinction law affects the conclusion, such as the photometric distances and age determination of the clusters from comparison with theoretical isochrones. All these shortcomings therefore make it difficult to understand the formation and early phase evolution of such objects. The interaction of large radiation fields of massive stars with dense molecular gas produce photodissociation regions (PDRs), which is an important tool to understand the star formation, as evolution of nearby dense cloud is primarily governed by these interactions. The interaction of shock generated by the massive stars may also be responsible for triggering further star formation within the molecular clouds in which they are born (Elmegreen & Lada 1977).

In this paper we have studied the Sh 2-294/RCW3 region ($\alpha = 07^{\mathrm{h}}16^{\mathrm{m}}34.5^{\mathrm{s}}, \delta = -09°26'38''$; J2000.0), which was identified as an H II region (Sharpless 1959) and is part of Monoceros cloud complex. In the optical, it appears like a butterfly with two wings separated by dark lane, roughly east-west. In the center of dark lane, a B0.5 star is detected (Moffat et al. 1979). Nondetection of H$_2$O maser in the search by Henkel et al. (1986) for the Sh 2-294 region indicates that the region is an evolved H II region. The radio map obtained by Felli et al. (1978) at 4.99 GHz shows good morphological agreement between the nebulosities in optical and radio up to a linear size of 7'. The molecular cloud associated with Sh 2-294 has been observed in CO (Blair et al. 1975; Blitz et al. 1982). In the literature the distance to Sh 2-294 ranges from 2.5 to 4.6 kpc, as quoted by Felli & Harten (1981). The Sh 2-294 region is coincident with an *IRAS* Point Source Catalog (PSC) source (IRAS 07141−0920), with an increasing spectrum from 12 to 100 μm. Wouterloot & Brand (1989) reported kinematic distance to the IRAS 07141−0920 as 3.01 kpc and a luminosity of $3.6 \times 10^3\, L_\odot$ for this *IRAS* source.

To continue our multiwavelength investigations of massive star-forming regions (see Ojha et al. 2004a, 2004b, 2004c; Tej et al. 2006), we have carried out a detailed study of Sh 2-294 as a useful example for understanding the massive star formation with the following layout of the paper. In § 2 we describe our observations and the reduction procedures. In § 3 we discuss other available data sets used in the present study. Section 4 discusses the stellar component and deals with the basic parameter determinations of the cluster associated with the massive star. Section 5 describes the interstellar matter (ISM) component and the physical environment associated with the massive star. Section 6 is devoted to a discussion a star formation scenario for the Sh 2-294 region, and in § 7 we present a summary of our results.

2. OBSERVATIONS AND DATA REDUCTION

2.1. *Optical Photometry*

$UBV(RI)_c$ CCD photometric observations were performed for the Sh 2-294 region on 2005 December 26 and 2006 March 6,

[1] Aryabhatta Research Institute of Observational Sciences, Nainital, 263129, India.
[2] Institute of Astronomy, National Central University, Chung-Li 32054, Taiwan.
[3] Tata Institute of Fundamental Research, Mumbai (Bombay), 400005, India.
[4] National Center for Radio Astrophysics, Post Bag 3, Ganeshkhind, Pune 411007, India.
[5] Indian Institute of Astrophysics, Koramangala, Bangalore 560 034, India.

using the $2K \times 2K$ CCD system at the f/13 Cassegrain focus of the 104 cm Sampurnanand Telescope (ST) of ARIES, Nainital (India). The 0.37 arcsec pixel^{-1} plate scale gives a field of view (FOV) of $12.6' \times 12.6'$ on the sky. The readout noise for the system was $5.3\ e^-$, while the gain was $10\ e^-$ per ADU. To improve the signal-to-noise ratio (S/N), observations were made in 2×2 pixel binning mode. Several bias frames and twilight flat-field exposures were taken during the observation. We observed the standard area SA101 (Landolt 1992) on 2006 March 6 several times during the night for the purpose of the determination of atmospheric extinction coefficients and for the photometric calibration of the CCD systems. The log of observations is given in Table 1. The CCD images were flattened using twilight sky flats, and bias subtraction was done using the IRAF[6] data reduction package. Then, for a given filter, frames of same exposure time were combined into one, to improve the S/N enabling us to detect fainter stars. The photometric measurements of the stars were performed using DAOPHOT II profile-fitting package of MIDAS. The stellar images were well sampled, and a variable PSF was applied from several uncontaminated stars present in the frames. The photometric errors at brighter magnitude levels ($V \leq 15$) are ~ 0.01 mag, which increases with V magnitude and become large (~ 0.1 mag) at $V \sim 22.5$ mag. The image parameters (e.g., `chi` and `sharpness`) and errors provided by DAOPHOT were used to reject poor measurements, and only the stars having error in magnitudes ≤ 0.1 are used in the further analyses.

2.2. *Optical Spectroscopy*

To study further, a spectroscopic observation was made on 2006 March 16 for one of the sources, possibly responsible for the ionization of Sh 2-294 (see Moffat et al. 1979; § 4.3). We used the Himalaya Faint Object Spectrograph Camera (HFOSC) available with the 2.01 m Himalayan *Chandra* Telescope (HCT), operated by the Indian Institute of Astrophysics, Bangalore (India). The instrument is equipped with a SITe $2K \times 4K$ pixel CCD. The central $2K \times 2K$ region, used for imaging, corresponds to a FOV of $\sim 10' \times 10'$, with a pixel size of $0.296''$. The slit spectra in the wavelength range, 3700–6800 Å, were obtained using low-resolution grism 7 with a slit width of $\sim 2''$. The spectroscopic observations were carried out under good photometric sky conditions. Bias and flat frames were obtained at the beginning and end of the observations. The one-dimensional spectra were extracted from the bias-subtracted and flat-field-corrected images using the optimal extraction method. Wavelength calibration of the spectra was done using FeAr lamp source.

2.3. *Optical and NIR Narrowband Imaging*

Optical CCD narrowband images of the nebula around Sh 2-294 were obtained in Hα filter ($\lambda = 6565$ Å, $\Delta\lambda = 80$ Å) and its nearby continuum filter ($\lambda = 6650$ Å, $\Delta\lambda = 80$ Å) using 104 cm telescope at ARIES, on 2006 September 28. Narrowband near-infrared (NIR) observations were carried out in the rotational-vibrational line of molecular hydrogen—H$_2(1\text{–}0)S1$ ($\lambda = 2.122\ \mu$m, $\Delta\lambda = 0.019\ \mu$m) and K continuum ($\lambda = 2.264\ \mu$m, $\Delta\lambda = 0.054\ \mu$m) with HCT on 2005 November 28 using the NIR imager (NIRCAM), which is a 0.8–2.5 μm camera with 512×512 HgCdTe array. For our observations, the NIRCAM was used in the Camera-B mode, which has a FOV of $\sim 3.6' \times 3.6'$. We obtained several dithered (by $20''$) frames of the target in order to remove bad pixels and cosmic rays, and to eliminate the presence

TABLE 1
Log of Observational Data

Date (UT)	Filter	No. of Frames	Exposure (s frame^{-1})
2005 Dec 26	U	3	1200
2006 Mar 6	U	2	300
2005 Dec 26	B	3	600
2006 Mar 6	B	2	240
2005 Dec 26	V	3	600
2006 Mar 6	V	2	180
2005 Dec 26	R	3	300
2006 Mar 6	R	2	120
2005 Dec 26	I	3	300
2006 Mar 6	I	2	80
2006 Sep 28....................	Hα	1	900
2006 Sep 28...................	Hα cont	1	900
2005 Nov 28...................	H$_2$	21	90
2005 Nov 28...................	K cont	21	30

of objects with extended emission for construction of sky images. All images were bias-subtracted and flat-field-corrected in the standard manner using IRAF package. The final images are produced by subtraction of continuum images after aligning and PSF matching.

2.4. *Radio Continuum Observation*

In order to probe the ionized gas component, radio continuum interferometric observation at 1280 MHz was conducted on 2006 December 8, using the Giant Metrewave Radio Telescope (GMRT) array. The GMRT has a Y-shaped hybrid configuration of 30 antennas, each 45 m in diameter. There are six antennas along each of the three arms (with arm length of ~ 14 km). These provide high angular resolution (longest baseline ~ 25 km). The rest of the 12 antennas are located in a random and compact 1×1 km^2 arrangement near the center and is sensitive to large-scale diffuse emission (shortest baseline ~ 100 m). The observations near 1280 MHz were made using the full 16 MHz bandwidth. Details of the GMRT antennae and their configurations can be found in Swarup et al. (1991). The source, 3C 147, was used as the primary flux calibrator, while the source 0432+416 was used as a secondary calibrator to derive the phase and amplitude gains of the antennae. The data analysis was done using AIPS. The corrupted data (dead antennae, interference, spikes, etc.) were identified using tasks IBLED, UVPLT, and VPLOT. The flagging of the bad data was carried out using UVFLG and TVFLG. The image of the field was formed by Fourier inversion and cleaning algorithm (IMAGR).

3. OTHER AVAILABLE DATA SETS

3.1. *Near-Infrared Data from 2MASS*

To complement our optical and NIR imaging data we have used the data for point sources around Sh 2-294 from the Two Micron All Sky Survey[7] (2MASS) Point Source Catalog (Cutri et al. 2003) in the J (1.25 μm), H (1.65 μm), and K_s (2.17 μm) bands. The 2MASS data have positional accuracy of better than $2''$. Our source selection was based on the "read flag," which gives the uncertainties in the magnitudes. To discuss the radial density profile of the cluster (see § 4.1) associated with the Sh 2-294

TABLE 2
Flux Density Details of the *MSX* and *IRAS* Point Sources

	Flux Density (Jy) for Fλ (μm)							
	1. *IRAS* HIRES Image[a] 2. *IRAS* PSC				*MSX* PSC			
Source	100	60	25	12	21.3	14.7	12.1	8.3
IRAS 07141−0920	240.30	125.50	18.03	10.00	...	...	...	...
	262.40	77.55	7.17	2.82	...	...	...	...
MSX6C G224.1880+01.2407............	...	...	...	...	3.40	0.86	1.90	0.88

[a] Fluxes obtained by integrating over a circular region of diameter 3′ centered on the peak.

region, we used 2MASS sources with "read-flag" values of 1–6 from our sample. However, to further improve the analysis, only sources with "read-flag" values of 1–3 have been used to study the 2MASS color-color (CC) and color-magnitude diagrams (CMDs; § 4.6). It is also to be noted that we used 2MASS images for astrometric purposes of our optical images with matching tolerance of 1.0″.

3.2. *Mid-Infrared Data from MSX*

The *Midcourse Space Experiment*[8] (*MSX*) surveyed the entire Galactic plane within $|b| \leq 5°$ in four mid-infrared (MIR) bands centered at 8.28 μm (A), 12.13 μm (C), 14.65 μm (D), and 21.34 μm (E) at a spatial resolution of 18.3″ (Price et al. 2001) and a global absolute astrometric accuracy of about 1.9″ (Egan et al. 2003). The MIR data are useful to study the large-scale distribution of warm ($\sim$1000 K) dust and emission from polycyclic aromatic hydrocarbons (PAHs). The *MSX* A (50% peak response range: 6.8–10.8 μm) and C (11.1–13.2 μm) bands include several PAH features at 6.2, 7.7, 8.7, 11.3, and 12.7 μm. Point sources have been selected from *MSX* Point Source Catalog version 2.3 (Egan et al. 2003) and *MSX* A-band image is used to see PAH emission around Sh 2-294. The flux densities of the *MSX* point source associated with Sh 2-294 are given in Table 2 and used for constructing the spectral energy distribution (SED).

3.3. *Mid- and Far-Infrared Data from IRAS HIRES*

The data from the *Infrared Astronomical Satellite* (*IRAS*) survey in the four bands (12, 25, 60, and 100 μm) for the region around Sh 2-294 were HIRES-processed (Aumann et al. 1990) at the Infrared Processing and Analysis Center (IPAC), Caltech, to obtain high angular resolution maps. Apart from determining the flux densities, the *IRAS* HIRES maps have been used to generate the dust color temperature and optical depth maps of interstellar dust. The integrated flux densities of the *IRAS* PSC associated with Sh 2-294 are given in Table 2.

4. INFRARED AND OPTICAL PROPERTIES OF STELLAR SOURCES

The Hα+continuum image and a false *JHK$_s$* color composite infrared image (*J*, *blue*; *H*, *green*; and *K$_s$*, *red*) of Sh 2-294 are shown in the left and right panels of Figure 1, respectively. A close-up view of *JHK$_s$* image reveals that there are two significant amounts of stellar density enhancements in the region. The eastern

region is situated at the border of Hα emission, hence the region of interest of this study.

4.1. *Radial Profile and Stellar Surface Number Density*

Sh 2-294 is listed as a partially embedded infrared cluster in the catalog compiled by Bica et al. (2003). To determine the boundaries of the cluster, we performed direct star counting, assuming spherical symmetry. We have selected sources that are detected in the 2MASS K_s band. To estimate the cluster radius we selected a region of 300″ centered on IRAS 07141−0920 source. The center of the cluster was estimated by convolving a Gaussian kernel with the stellar distribution and taking the point of maximum density as the center. This was performed for both the axes to get the central coordinates of the cluster. The center was found to be at $\alpha = 07^h16^m33^s$, $\delta = -09°25'35''$ (J2000.0). To determine the radial surface density, the Sh 2-294 region was divided into a number of concentric rings from the cluster center. The projected radial stellar density in each concentric circle was obtained by dividing the number of stars in each annulus by its area. The error bars are derived assuming that the number of stars in each annulus follow Poisson statistics. To account for the contribution from the field stars, we selected a control field ($\alpha = 07^h17^m33^s$, $\delta = -09°25'24''$; J2000.0), which is $\sim$15′ to the east of IRAS 07141−0920 source. Figure 2 shows the radial density profile of the cluster (*open circles*), and the horizontal dashed line shows field star density estimated from the control field. A clear gradient in surface number density distribution of the Sh 2-294 region confirms the existence of clustering around the center of the region. Several studies have shown that the radial density profiles of young embedded clusters can be fitted by both the inverse radius (r^{-1}) model and the King's model (e.g., Horner et al. 1997; Teixeira et al. 2004; Baba et al. 2004). Neglecting the tidal radius, the King's profile can be written as

$$f(r) = a + \frac{f_0}{1 + (r/r_c)^2}, \qquad (1)$$

where r_c is the core radius (the radius at which the surface density falls to half of the central density f_0) and a is the constant for background offset due to field stars.

For the Sh 2-294 cluster, we found that the King's model has a better fit (reduced $\chi^2 = 0.96$) as compared to "r^{-1}" model (reduced $\chi^2 = 1.04$). Within errors, the King's profile (Fig. 2, *dotted curve*) merges with the background field at $\sim$2.3′, which corresponds to $\sim$3.2 pc at a distance of 4.8 kpc (see § 4.5). We take this as the cluster radius. The background level as estimated from the control field is $\sim$4.7 stars arcmin^{-2}, which is in reasonable agreement with the value of $\sim$3.8 stars arcmin^{-2} obtained from King's profile.
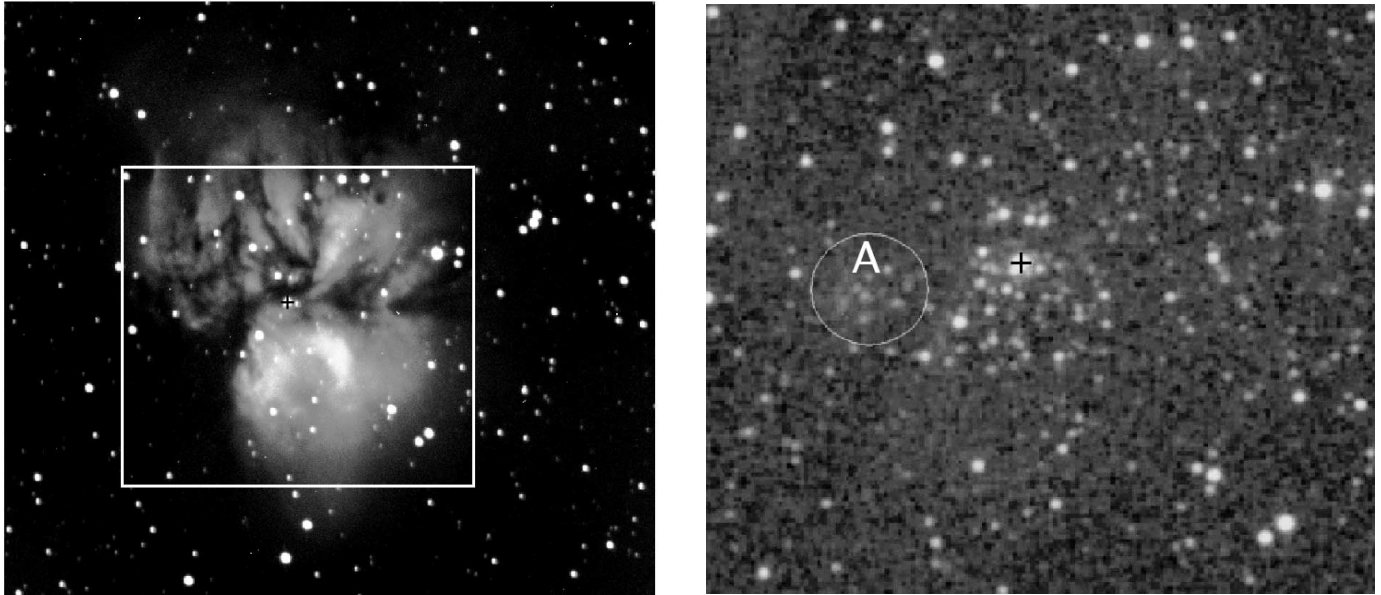
FIG. 1.—*Left*: Hα+continuum image (∼9.7′ × 8.6′) of the ionized gas associated with the Sh 2-294 region. The box in the Hα image shows the FOV of the NIR image shown in the right panel. *Right*: Corresponding JHK_s color composite image (∼5.1′ × 4.7′) from 2MASS data. North is up, and east is to the left. The circle in the NIR image indicates the young embedded cluster at the border of the H II region (see text for details). The plus sign in both images mark the position of the possible exciting source of Sh 2-294 (see § 4.3). [*See the electronic edition of the Journal for a color version of this figure.*]

The contour map of the stellar surface number density (SSND) around Sh 2-294 was made using kernel method (Gomez et al. 1993; Silverman 1986) and is shown in Figure 3. The stellar density distribution is smoothened by 12″ × 12″ sampling box. At the distance of 4.8 kpc, the unit cell corresponds to ∼0.28 × 0.28 pc. The contour levels are drawn from 3 times of the background level with an increment of 2 stars pc^{-2}, where the background level is taken as 4 stars arcmin^{-2} (2 stars pc^{-2}). The peak of the projected stellar density distribution was found to be $\alpha = 07^h16^m33^s$, $\delta =$
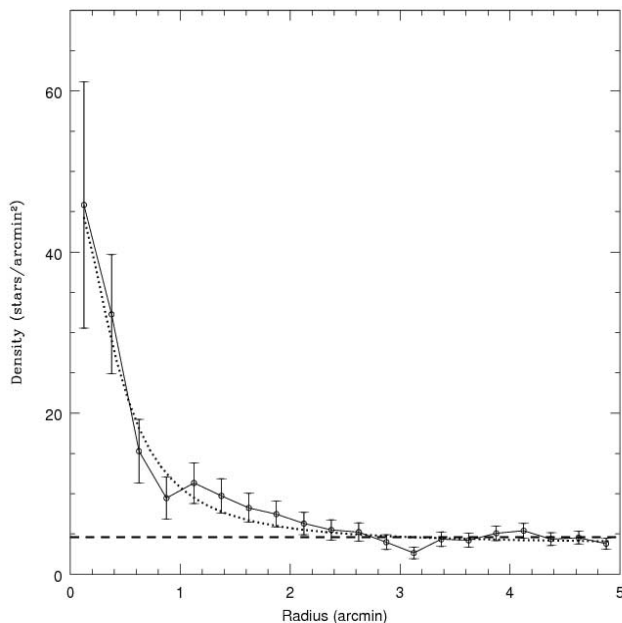

FIG. 2.—Surface number density profile as a function of radius for the sources associated with Sh 2-294. The fitted King's profile (*dotted line*) and the radial variation of projected stellar density (*solid line*) indicate that the cluster is confined within 2.3′ radius. The error bar represents $\pm N^{1/2}$ errors. The horizontal dashed line represents the density of field stars.

$-09°25'29''$, which is close (6″) to the position found by convolving a Gaussian kernel as discussed above. The King's profile fitting yields a central density of 44 ± 13 stars arcmin^{-2} (∼22 stars pc^{-2}), correlates well with ∼22 stars pc^{-2} of the peak of SSND. The clustering in the central region is more obvious in the surface density map. However, there is evidence that Sh 2-294 possesses distinct substructures. The substructures in the east and northwest directions indicate the density enhancement, which can also be seen as a second peak in radial density distribution around ∼1.2′ from the central peak (see Fig. 2). The eastern substructure is roughly spherical in shape and more prominent with peak approximately at $\alpha = 07^h16^m38^s$ and $\delta = -09°25'40''$, having central density of 13 stars pc^{-2}. This substructure is at a distance of ∼1.23′ from the cluster center of Sh 2-294 and is also located beyond the faintest nebulosity associated with the central cluster seen in the 2MASS K_s-band image. Therefore, it might be another independent cluster but still embedded in the molecular cloud complex harboring Sh 2-294. Hereafter, we refer to this region as "region A" for our further discussion in the paper. In Figure 1 (*right*) region A is represented by a white circle in a JHK_s color composite image.

4.2. *Probable Members of the Cluster*

To study the various parameters of the cluster, it is necessary to remove field star contamination from the sample of stars in the cluster region. Membership determination is also crucial for assessing the presence of PMS stars, because both PMS stars and dwarf foreground stars occupy similar positions above the zero-age main sequence (ZAMS) in the CMD. In the absence of proper motion, we used statistical criterion to estimate the number of probable field stars in the cluster region by selecting a control region of same area from our CCD image (control field is used to estimate the field star contamination). Figures 4a and 4b show $V, (V − I)$ CMDs for the cluster and control field regions, respectively. The contamination due to background field population is clearly visible in the cluster region CMD. To remove contamination of field stars from the cluster region sample, we statistically subtracted the contribution of field stars from the CMD of the
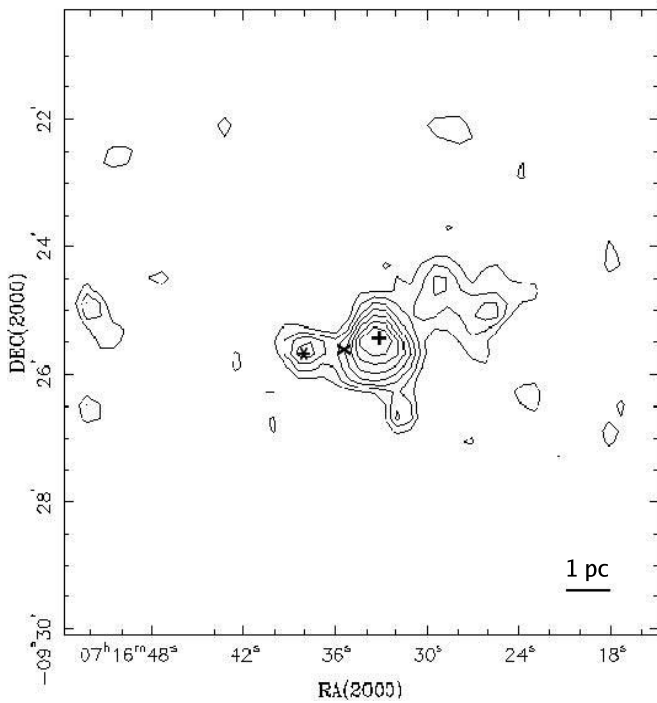
FIG. 3.—Contour map of the stellar surface number density obtained by counting stars in a $12'' \times 12''$ ($\sim 0.28 \times 0.28$ pc) grid for the cluster associated with Sh 2-294. The contours are drawn from 6 to 22 stars pc^{-2} in steps of two stars pc^{-2}. The lowest contour is at 3 times of the background level. The positions of the *MSX* and *IRAS* point sources are marked with an asterisk and a cross, respectively. The plus sign represents the possible exciting star of the region.

cluster region following the procedure given by Mateo & Hodge (1986). For a randomly selected star in the $V, (V - I)$ CMD of the field region, the nearest star in the cluster's $V, (V - I)$ CMD within $V \pm 0.25$ and $(V - I) \pm 0.125$ of the field star was removed. The statistically cleaned $V, (V - I)$ CMD of the cluster region is shown in Figure 4c, which clearly shows the presence of PMS stars in the cluster. The presence of a few field stars in the sta-
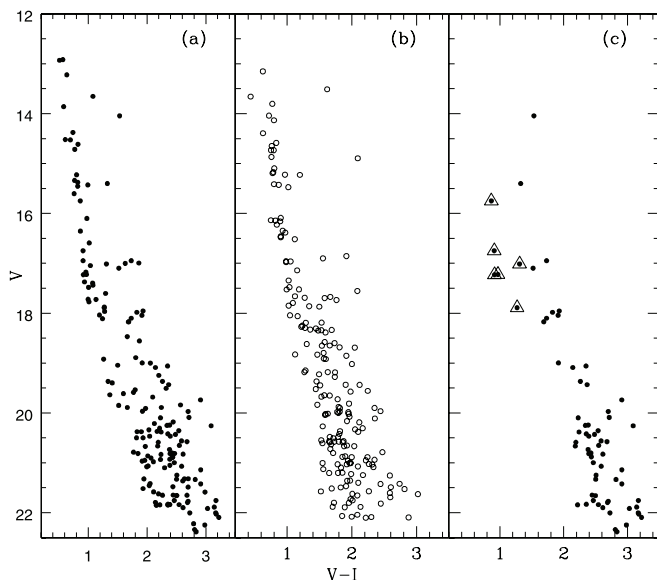

FIG. 4.—$V, V - I$ CMDs for (a) stars in the cluster region, (b) stars in the nearby field region of same area as of cluster region, and (c) statistically cleaned CMD, where the points with triangles are probable field stars (see § 4.4).
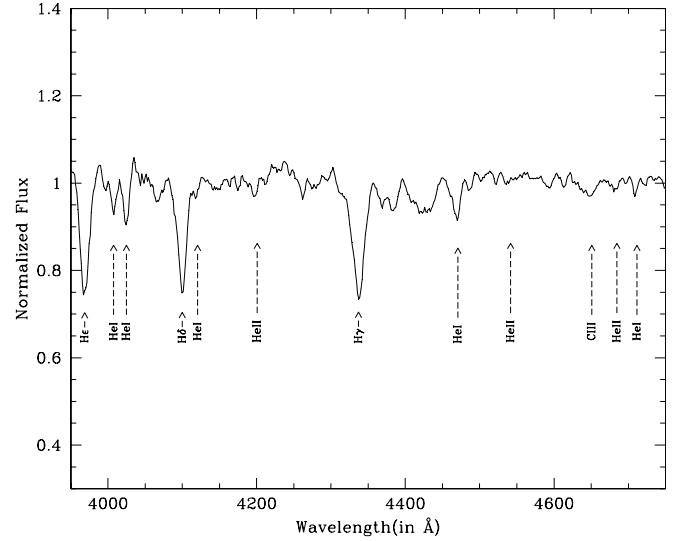

FIG. 5.—Blue part of the spectrum for the ionizing source of Sh 2-294. The spectrum displays characteristics similar to those of B0 ± 0.5 V MS members.

tistically cleaned CMD can still be noticed. These probable field stars are identified by using the CC diagram and marked as triangles in Figure 4c, as well as in Figure 6 (see § 4.4).

4.3. Spectral Type of Ionizing Source

The brightest member found in our statistically cleaned CMD is situated at the center of optical nebula having $\alpha = 07^{h}16^{m}33^{s}$, $\delta = -09°25'22''$. The photometric spectral type of this star is of B0.5, with $V = 13.99$ and $B - V = 1.03$, which is the source of ionization in Sh 2-294 (Moffat et al. 1979). This is in agreement with our measurements, $V = 14.04$, $B - V = 1.04$, and $M_V = -3.56$ at the assumed distance 4.8 kpc (see § 4.5), correspond to B0.5 V spectral type (Schmidth-Kaler 1982; Panagia 1973). The second brightest member of the cluster has $V = 15.41$ and $M_V = -2.20$, which is consistent with spectral type between B2–B3 V (Schmidth-Kaler 1982; Panagia 1973). As stars of spectral type B2 or earlier are known to produce a significant proportion of their radiation as photons with energy high enough to form H II region; therefore, the star situated at the center is most probably the ionizing source of the Sh 2-294 H II region.

To determine the spectral type of this ionizing source, we extracted one-dimensional spectrum (see § 2.2), with aperture centered on the star. Figure 5 shows the spectrum of the star in the range 3950–4750 Å. Besides hydrogen Balmer lines (H$_\gamma$, H$_\delta$, H$_\epsilon$, etc.), the spectrum displays He II line at $\lambda \sim 4200$ Å, and weak He II line at 4686 Å, along with O II/C III blend at $\approx$4650 Å, indicates that the spectral type of the star is earlier than B1. Specifically He II line at λ4200 Å is seen in stars of spectral type B0.5–B0.7 or earlier. On the other hand, the weakness of He II line at λ4541 Å relative to the He I line at 4471 Å indicates an spectral type latter than O9, while He II λ4686 $\lesssim$ He I λ4713 favors the classification of $\sim$B0. Comparing the composite spectrum with that in the atlas of low-resolution stellar spectra of Jacoby et al. (1984) and with the atlas of Walborn & Fitzpatrick (1990), we propose that the exciting source for Sh 2-294 has an equivalent spectral type of B0 ± 0.5 V.

4.4. Extinction

The extinction in star cluster arises due to two distinct sources: (1) the general ISM in the foreground of the cluster [$E(B-V)_{\min}$], and (2) the localized cloud associated with the cluster

$[\triangle E(B - V) = E(B - V)_\star - E(B - V)_{\min}]$, where $E(B - V)_\star$ is the reddening of the star embedded in the parent cloud. The former component is characterized by the ratio of the total to the selective extinction $R_V [= A_V/E(B - V)] = 3.1$ (Wegner 1993; He et al. 1995; Winkler 1997), whereas for the intracluster regions of young clusters embedded in dust and gas cloud the value of R_V varies significantly (Tapia et al. 1991; Pandey et al. 2003). However, H II regions associated with a large amount of gas and dust often show larger values of R_V (Forte 1978; The & Groot 1983; Chini & Wargau 1990; Pandey et al. 2000).

In the absence of spectroscopic observation, the interstellar extinction $E(B - V)$ toward the cluster region can be estimated using the $(U - B)/(B - V)$ CC diagram. The CC diagram of the cluster region is presented in Figure 6, which contains data points for all the stars having $V \leq 18$ mag. The figure clearly shows a large amount of contamination due to foreground stars. The probable field stars in the statistically cleaned CMD follow the sequence of foreground stars and are marked as triangles in Figure 6. The probable cluster members manifest a more reddened sequence than the foreground sequence. To match the observations, the ZAMS by Schmidt-Kaler (1982) is shifted along the reddening vector having a normal slope of $[E(U - B)]/[E(B - V)] = 0.72$. The CC diagram indicates that the foreground population is reddened by $E(B - V) = 0.2$ mag. The minimum reddening for the cluster region is estimated to be $E(B - V)_{\min} = 1.35$ mag.

4.4.1. Ratio of the Total to the Selective Extinction

The variable amount of absorbing grains in the line of sight determines the total extinction toward each star. In practice, the color excess for a star is obtained by comparing its intrinsic color with the observed color, and the total visual extinction is derived by using the shape of dust-reddening law. The direct method, however, cannot be easily applied because the intrinsic colors of most of the stars are usually unknown, so that an indirect way of statistical approach can be adopted on the basis of number of stars detected in the investigated region. It has been shown by Chini & Wargau (1990) that two-color diagrams (TCDs) of the form of $(V - \lambda)$ versus $(B - V)$, where λ is one of the wavelengths of the broadband filters (R, I, J, H, K), provide an effective method of separating the abnormal extinction arising within such clusters from the normal extinction produced by general ISM. Chini & Wargau (1990) and Pandey et al. (2000) used TCDs to study the anomalous extinction law in the clusters M 16 and NGC 3603, respectively.

To construct TCDs, we used the probable cluster members obtained from statistically cleaned CMD (see § 4.2). The stars showing infrared excess are not included in the analysis. Figure 7 shows the $(V - \lambda)/(B - V)$ TCDs for all the probable members of the cluster region. The slopes of the distribution are obtained by using the weighted least-squares fit to the data points. To derive the value of R_{cluster} (ratio of the total to the selective extinction in the cluster region), we use the approximate relation (see Neckel & Chini 1981)

$$R_{\text{cluster}} = \frac{m_{\text{cluster}}}{m_{\text{normal}}} R_{\text{normal}}. \qquad (2)$$

Here m_{cluster} and m_{normal} are the slopes of the distribution followed by cluster stars and normal MS stars (taken from the stellar models by Bertelli et al. 1994), respectively. The slopes are given in Table 3. The R_{normal} represents to the value of 3.1. The weighted mean value of R_{cluster} comes out to be 3.8 ± 0.1, indicating an anomalous reddening law for the Sh 2-294 region.
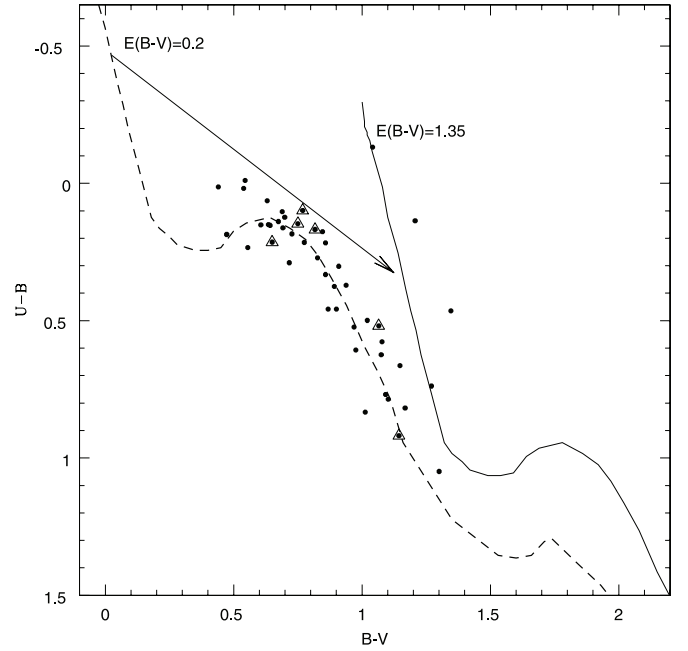

Fig. 6.—Color-color ($U - B/B - V$) diagram for the stars lying within the cluster radius. The dashed and continuous curves represent the intrinsic MS for $Z = 0.02$ by Schmidt-Kaler (1982) shifted along the reddening vector of slope 0.72 (arrow) for $E(B - V)_{\text{mean}} = 0.2$ mag and slope $E(B - V)_{\min} = 1.35$ mag, respectively. The points with triangles are likely to be probable field members identified in statistically cleaned CMD (see Fig. 4c).

Here we would like to mention that the value of R_{cluster} obtained by using equation (2) should be considered as an approximate estimation of R in the cluster region.

To further test the reddening and R_V value, we used the observed properties of ionizing source and assumed that the spectral type of the star is B0 V. The observed V magnitude of the ionizing star is 14.04 with $B - V = 1.04$. Comparing with intrinsic colors of Johnson (1966), the reddening $E(B - V)$ to the star corresponds to 1.35 mag. The R_V value to the star can be calculated using the empirical relationship established by Whittet et al. (1976) between R_V, the color excesses $E(B - V)$ and $E(V - K)$,

$$R_V = 1.10 \times E(V - K)/E(B - V), \qquad (3)$$

To derive R_V for the star, the JHK_s magnitudes of the star are transformed from 2MASS system to Koornneef system using the relation given by Carpenter (2001) and intrinsic $V - K$ color obtained from Koornneef (1983). The R_V value thus obtained is ~ 3.9. Hence, the reddening and ratio of the total to the selective extinction estimated as above agree quite well with the value found from TCDs.

4.5. Distance and Age of Sh 2-294

The ages of young clusters are typically derived from post–main-sequence evolutionary tracks for the earliest members if significant evolution has occurred or by fitting the low-mass contracting population with theoretical PMS isochrones. The fitting of theoretical zero-age main sequence (ZAMS) to the observed sequence yields distance. The distance of the cluster associated with Sh 2-294 is derived using statistically cleaned CMDs as shown in Figure 8. Using the foreground reddening $E(B - V) = 1.35$ mag toward the cluster region and $E(V - R)/E(B - V) = 0.60$, we visually fitted the ZAMS (solid curve) given by Schmidt-Kaler
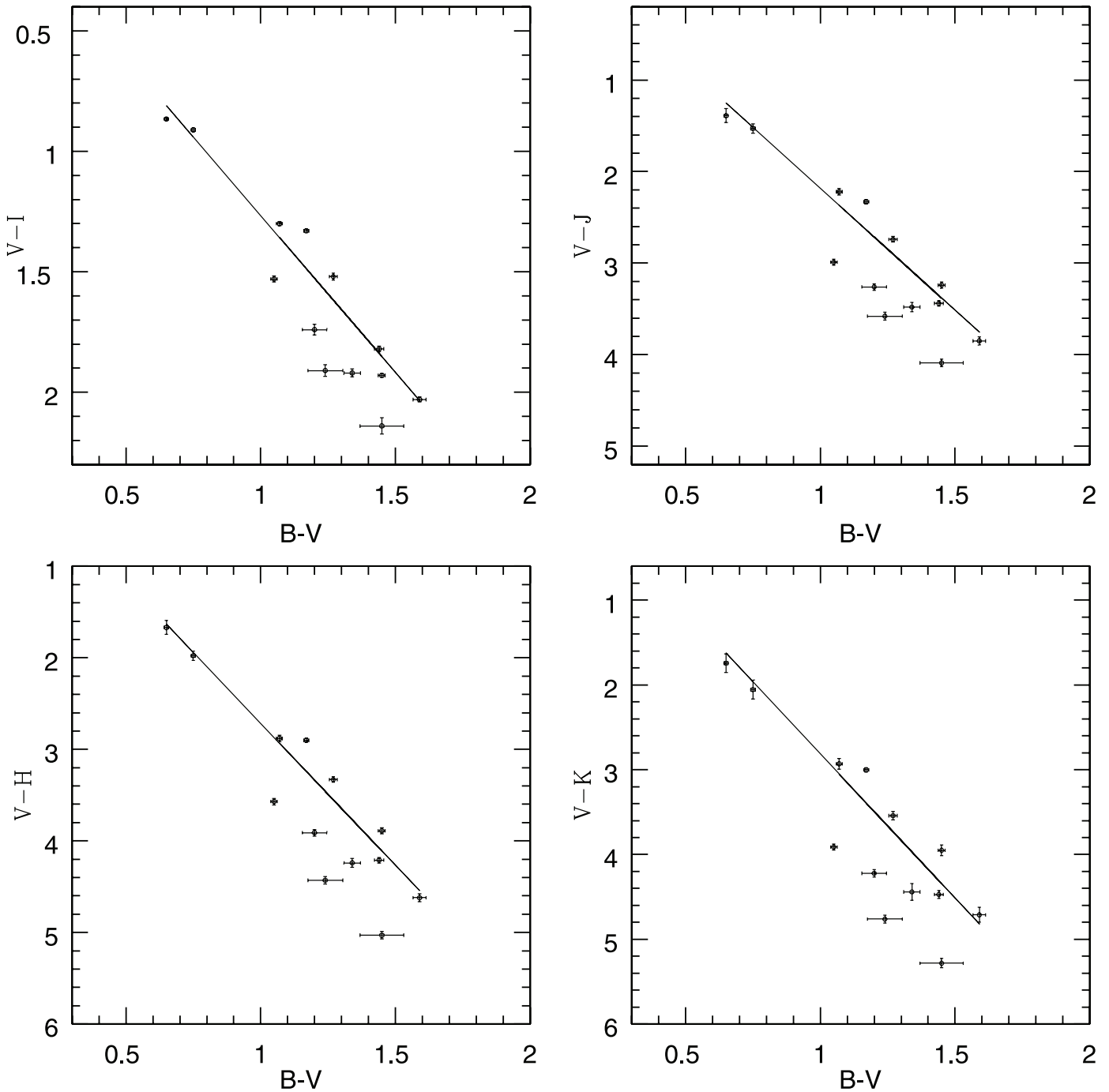
FIG. 7.—$(V − I)$, $(V − J)$, $(V − H)$, and $(V − K)$ vs. $(B − V)$ two-color diagrams for the probable cluster members found in statistically cleaned CMD. The straight line shows the weighted least-squares fit to the data.

TABLE 3
SLOPES OF STAR DISTRIBUTION IN SH 2-294

Color Ratio	$m_{cluster}$	m_{normal}
$(V − R)/(B − V)$	$−0.62 \pm 0.02$	$−0.55$
$(V − I)/(B − V)$	$−1.30 \pm 0.04$	$−1.10$
$(V − J)/(B − V)$..........................	$−2.67 \pm 0.07$	$−1.96$
$(V − H)/(B − V)$	$−3.10 \pm 0.08$	$−2.42$
$(V − K)/(B − V)$..........................	$−3.40 \pm 0.11$	$−2.60$

(1982) and Walker (1985) to the $V, B − V$ and $V, V − R$ CMDs, respectively. The visual fit yields a distance modulus of $(m−M)_V = 17.6 \pm 0.10$, which corresponds to a distance of 4.8 ± 0.2 kpc. Our distance estimation is in agreement with the most widely used distance of 4.6 kpc for this source. Theoretical isochrone for 4 Myr $(Z = 0.02)$ by Bertelli et al. (1994) is also shown in Figure 8. Since massive stars do not show significant evolution, a maximum age of 4 Myr can be expected for the cluster. In Figure 8 we have also overplotted PMS isochrones from Siess et al. (2000) for 1 and 5 Myr. The open circles with dots inside represent the optical counterpart of NIR excess stars (see § 4.6.1), which are the probable PMS sources of the cluster. The positions of these sources in the CMD indicate an age spread of 1–5 Myr.
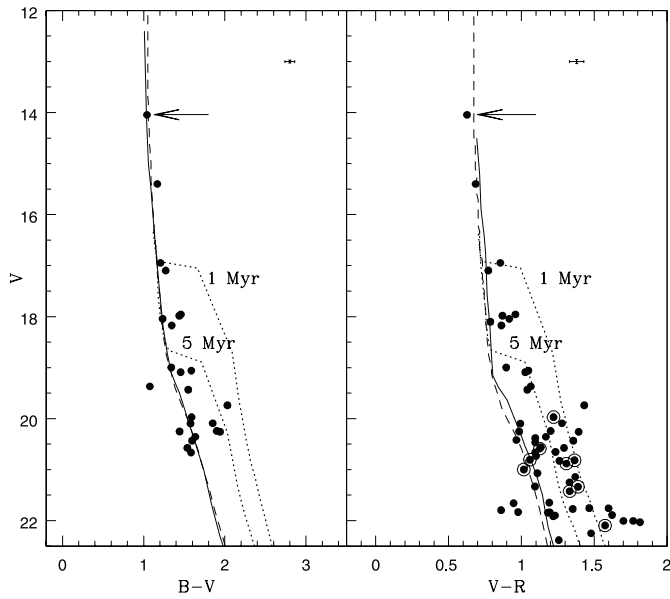
FIG. 8.—Field star decontaminated V, $B - V$ and V, $V - R$ CMDs for the stars within the cluster region. The probable field members identified in Figs. 4c and 6 are not included in these figures. The ZAMS in V, $B - V$ and V, $V - R$ CMDs (*solid curves*) are by Schmidt-Kaler (1982) and Walker (1985), respectively. The isochrone of 4 Myr (*dashed curve*) is by Bertelli et al. (1994), and the PMS isochrones for 1 and 5 Myr (*dotted curve*), by Siess et al. (2000), are plotted for $E(B - V)_{min} = 1.35$ mag and a distance modulus of 17.6 mag. The open circles with dots inside represent the optical counterparts of NIR excess stars (see § 4.6.1). The arrow points to the possible ionizing source of Sh 2-294. The average photometric errors are shown in the top right corner of the diagrams.

4.6. Nature of Sources Associated with Sh 2-294

In JHK_s color composite image (see Fig. 1 *right*), one could see that region A is significantly redder than other parts of the region. The sources in this region have no optical counterpart implying that they are still deeply embedded in the molecular cloud of high visual extinction.
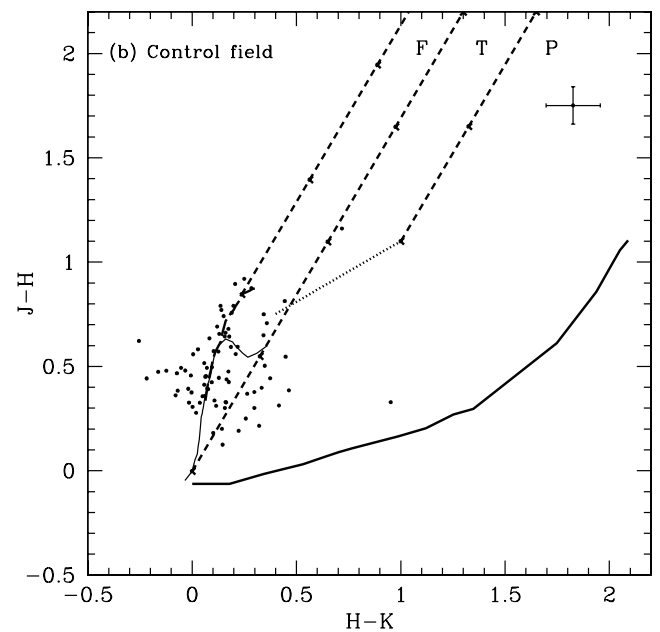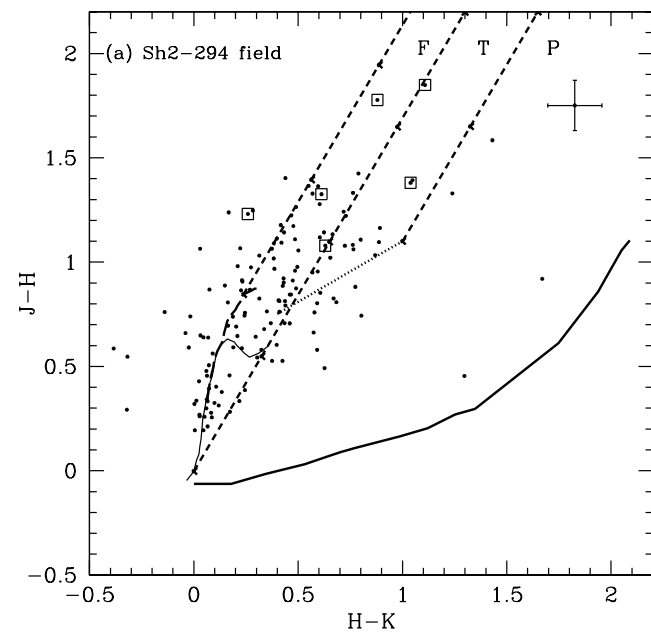
4.6.1. NIR Color-Color Diagram

In order to examine the nature of the stellar population, we use $(H - K)$ versus $(J - H)$ CC diagrams of the Sh 2-294 star-forming region and the control field. In Figure 9 we have plotted 141 and 79 sources for the cluster region and the control region, respectively, having 2MASS "read-flag" values of 1–3 (good quality photometric magnitudes) in all the three JHK_s bands. To plot the stars in the CC diagrams, we transformed the magnitudes and colors to the CIT system. The solid thin curve represents the locus of MS, and the thick-dashed curve is for giant stars taken from Bessell & Brett (1988). The dotted line represents the classical T Tauri (CTT) locus as determined by Meyer et al. (1997). The thick solid curve represents the Herbig Ae/Be locus (Lada & Adams 1992). Presuming universal nature of the extinction law in NIR region (Mathis 1990), we plotted reddening vectors of the normal reddening law as parallel dashed lines. We assumed that $A_J/A_V = 0.265$, $A_H/A_V = 0.135$, $A_K/A_V = 0.090$ for CIT system (Cohen et al. 1981).

The arrow in Figure 9a points to the position corresponding to the central brightest star in the cluster. We calculated the spectral type of the star by shifting it along the reddening vector to the intrinsic main-sequence locus. We found the spectral type of the brightest star in the cluster to be ∼B0. In Figure 9a we have shown the sources belonging to region A in squares; these are the sources in a circular area of radius 20″ around the second peak (eastern substructure) seen in the SSND diagram (see Fig. 3). Figure 9a shows that the average visual extinction ($A_V \sim 7.4$ mag) for the sources of region A is higher than the average A_V (∼3.3 mag) of the sources associated with other parts of the Sh 2-294 region. We have calculated the extinction by de-reddening the stars of region "F" (see below) in the CC diagram to the M0–M6 part of main-sequence locus. The high A_V indicates that the stars in region A are more deeply embedded thus suffers a higher extinction.

We have classified the CC diagram into three regions (e.g., Sugitani et al. 2002; Ojha et al. 2004a, 2004b) to study the nature of sources. The F sources are located within the reddening band of the MS and giant stars. These stars are generally considered to

FIG. 9.—$(H - K)$ vs. $(J - H)$ color-color diagrams for (*a*) the cluster region in Sh 2-294 and (*b*) the control region. The locus of the main sequence (*thin solid curve*) and giant branch (*thick dashed curve*) are from Bessell & Brett (1988). The dotted line represents the locus of classical T Tauri stars (from Meyer et al. 1997). The parallel dashed lines are the reddening vectors, with crosses along the lines corresponding to visual extinction of 5 mag. The thick continuous curve represents the locus of Herbig Ae/Be stars (Lada & Adams 1992). The open squares with dots represent the sources located in region A. The plot is classified into three regions, namely, F, T, and P for different classes of sources (see text for details). The average photometric errors are shown in the top right corner of the diagrams.

be either field stars, Class III objects, or Class II objects with small NIR excess. "T" sources are located redward of region F, but blueward of the reddening line projected from the red end of the CTT locus of Meyer et al. (1997). These sources are considered to be mostly T Tauri stars (Class II objects) with large NIR excess. "P" sources are those located in the region redward of region T, and are most likely Class I objects (protostellar objects). There may be an overlap in the NIR colors of the upper end band of Herbig Ae/Be stars and in the lower end band of T Tauri stars in region T (Hillenbrand et al. 1992).

The majority of sources in our sample are distributed in the F region. A total of 36 sources show NIR excess (i.e., sources right to the F region), out of which 18 sources are populating in the T and the P regions, characteristic of young stellar objects (YSOs) of Classes II and I. However, this is the lower limit, as several cluster members detected in the K_s band may not be detected in the other two shorter NIR wavelength bands. The fraction of NIR excess stars in a cluster is an age indicator because the disks/ envelopes become optically thin with the age. For young embedded clusters with age $\leq 1 \times 10^6$ yr the fraction is $\sim 50\%$ (Lada et al. 2000; Haisch et al. 2000) and the value is $\sim 40\%$, as in case of the YSOs in the Taurus dark clouds, which have an estimated age of about $\sim (1-2) \times 10^6$ yr (Kenyon & Hartmann 1995). The fraction decreases to $\sim 20\%$ for the clusters with age $\sim (2-3) \times 10^6$ yr (Haisch et al. 2001; Teixeira et al. 2004). We have detected six point sources in region A in all the three bands within the 2MASS detection limits. One of the sources located left of the reddening vector of giant stars (leftmost reddening vector in Fig. 9a) is probably a field star of the region, whereas two sources show NIR excess, characteristic of YSOs of Class II. The fraction of the NIR excess stars ($\frac{2}{5}$, 40%) in region A thus suggests an upper age limit of $\sim (1-2) \times 10^6$ yr of the cluster. We also found three 2MASS sources detected only in K_s band within region A (see § 6.1), which could be YSOs in their earliest stages still embedded in the cloud. The nondetection of these sources in J and H bands limits our analysis to examine the exact nature of each source. If we presume that these sources are YSOs having circumstellar disks, then the fraction of NIR excess stars ($\frac{5}{8}$, 62%) would suggest an age of $\leq 1 \times 10^6$ yr to region A. However, to further improve the statistics, observations in L and M band are needed. In the CC diagram of control field, most of the sources are spread over lower part of region; they are mainly foreground stars. In comparison, the distribution of sources in the cluster region shows a mixture of field stars and reddened sources probably having warm circumstellar dust, characteristic of young PMS objects (Lada & Adams 1992). In order to examine the statistical properties of the cluster sources, the histograms of $H - K$ colors are shown in Figure 10. The color distribution of sources belonging to control field is shown in shaded area, whereas for the cluster region the distribution is shown in thick lines. The histogram shows two peaks in the ranges $0.05 \leq H - K \leq 0.2$ and $0.35 \leq H - K \leq 0.5$ for the cluster region. The peak of $H - K$ color distribution of control region is ahead of cluster region in the range $0.05 \leq H - K \leq 0.2$. Hence, the first peak of $H - K$ color distribution of cluster region may be due to the foreground population of the region. On the other hand, a large number of sources were found in the cluster region with $H - K \geq 0.4$. The existence of these reddened sources indicates a population of young stars still embedded in significant quantities of intervening gas and dust.

4.6.2. NIR Color-Magnitude Diagram

Further information about the nature of the sources can be extracted from the $(J - H)$ versus J and $(H - K)$ versus K CMDs.
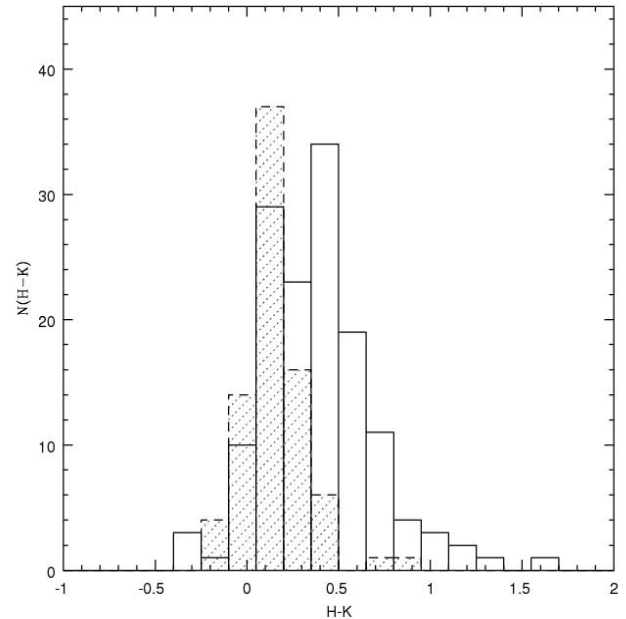

FIG. 10.—Frequency distribution of $H - K$ colors of the sources in the control field (*shaded area*) and the Sh 2-294 star-forming region (*thick solid line*).

In $(H - K)$ versus K CMD (Fig. 11) we have plotted all the 141 sources detected in the JHK_s bands plus an additional 11 sources that are detected in the H and K_s bands only. The vertical solid lines represent ZAMS curves (for a distance of 4.8 kpc) reddened by $A_V = 0$, 10, and 20 mag, respectively. The parallel slanting lines represent the reddening vectors to the corresponding spectral type. An apparent MS track is noticeable with $A_V \sim 1.5$ mag in this diagram; however, a comparison of it with a similar diagram for the stars in the control field shows that it is a false sequence caused by field stars in the foreground of Sh 2-294. The foreground sources in the cluster region are of $H - K < 0.2$. YSOs (Classes II and I) found from the CC diagram (Fig 9a) are shown as star symbols and filled triangles, respectively. The probable Herbig Ae/Be sources are shown as crosses, and the sources belonging to region A are shown as squares. Sources detected only in H and K_s bands that may also be YSOs are represented by large filled circles. For the sources detected in H and K_s bands, we have taken the K_s magnitude as $K_{\rm CIT}$ due to absence of appropriate transformation equation between $K_{\rm 2MASS}$ to $K_{\rm CIT}$ system but the colors are transformed to the CIT system. Out of 11 sources detected in H and K_s bands, only six show $H - K \geq 1.0$; hence they are probably young stars in their earliest evolutionary phases.

The mass of the probable YSO candidates can be estimated by comparing their locations on the CMD with evolutionary models of PMS stars. To minimize the effect of the "excess" emission in the NIR, we used $(J - H)$ versus J CMD instead of the $(H - K)$ versus K color-magnitude diagram to derive the ages and masses of the YSOs. Figure 12 represents intrinsic $(J - H)$ versus J CMD for probable YSOs (Classes II and I). The symbols are same as in Figure 11. To produce the intrinsic CMD, the extinction in front of YSOs are derived by tracing back along the reddening vector to the CTT locus or its extension in $(H - K)$ versus $(J - H)$ CC diagram (Fig. 9a). Here we would like to mention that the present derivation of extinction is an approximate approach. The thin solid line represents a PMS isochrone of 1×10^6 yr from Siess et al. (2000), at an assumed distance of 4.8 kpc. Arrow lines are the
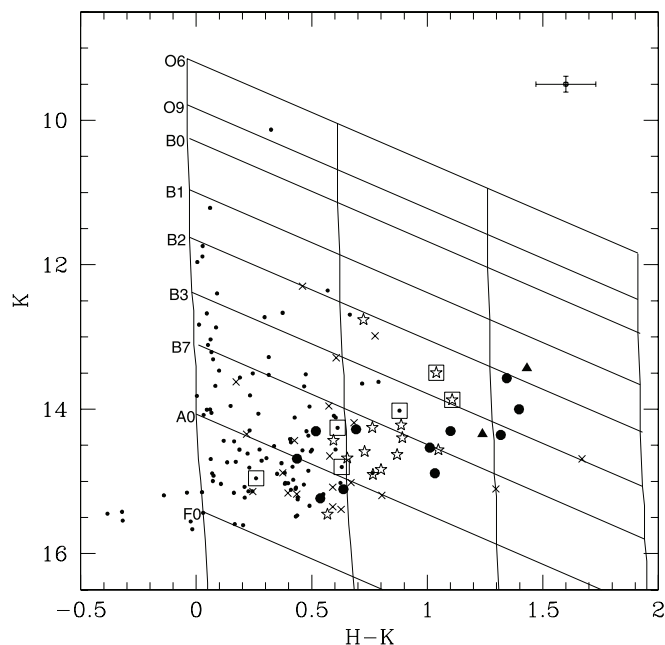
FIG. 11.—Color-magnitude diagram [$(H - K)$ vs. K] for sources detected in all the three 2MASS bands along with those detected only in H and K_s bands within the cluster radius. The thick vertical solid lines represent the ZAMS curves reddened by $A_V = 0$, 10, and 20 mag, respectively. The slanting lines trace the reddening vectors for each spectral type. Star symbols represent sources of T Tauri type (Class II), filled triangles represent protostellar (Class I) objects, crosses represent the probable Herbig Ae/Be stars, filled circles represent those sources detected in H and K_s band only, and squares represent the sources that lie in region A. The average photometric errors are shown in the top right corner of the diagram.

reddening vectors for sources with masses of 0.5 and 3.5 $M_\odot$, respectively, for 1×10^6 yr. As can be seen in Figure 12, the majority of YSOs have masses in the range of 0.5–3.5 $M_\odot$, indicating that these may be T Tauri stars.

5. DESCRIPTION OF THE H II REGION

5.1. *Emission from Ionized Gas*

Figure 1 shows the Hα+continuum image of Sh 2-294. The nebula looks loose bipolar in nature, having an elongated obscuring dark lane extending approximately in the east-west direction cutting across at the center. The obscuring dark lane at the center suggests the presence of a molecular cloud. Indeed, Blair et al. (1975) detected CO ($J = 1 \rightarrow 0$) emission over a $6' \times 6'$ area with peak in CO intensity at $\alpha = 07^h 16^m 32^s$, $\delta = -09°25'23''$. The lines were centered at $V_{\mathrm{LSR}} = +32$ km s^{-1}. The dark lane divides the nebula into two parts, with bright nebulosity to the south and less bright to the north, which decreases in surface brightness away from the obscured region. The southern component is brighter and has sharp arc structure in the east direction, giving an impression of a possible ionization front (IF). Whereas the northern component is more extended and very filamentary in structure, it gives a stunning view of the dust content of the region, proving that a significant amount of dust is concentrated in the stringlike filaments across the region. This structured feature suggests an inhomogeneous spatial distribution of the interstellar matter.

Felli & Churchwell (1972) reported the radio continuum emission from Sh 2-294 region in their low-resolution (half-power beamwidth = $10'$) 1.4 GHz survey of Galactic H II regions. Because of this resolution the object appeared featureless. However, the observation with VLA (Fich 1993) with resolution of
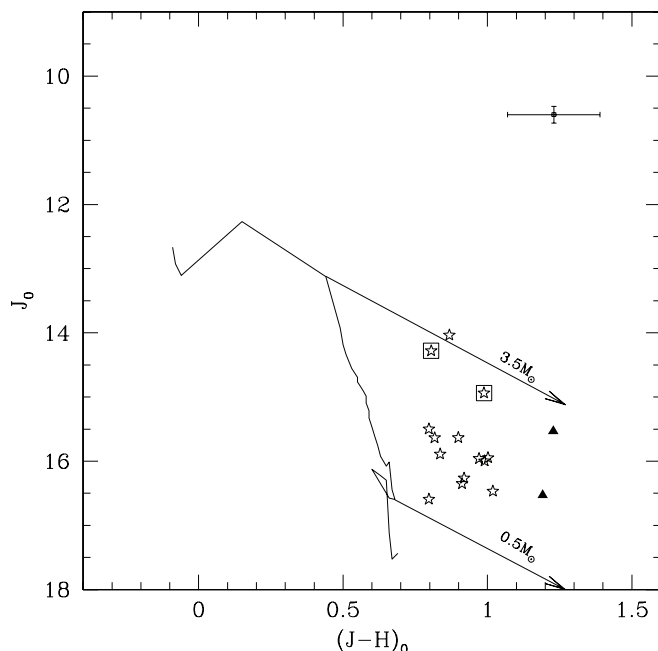

FIG. 12.—$(J - H)$ vs. J intrinsic CMD for the YSOs (Classes II and I) in the Sh 2-294 region. Stars are dereddened according to their individual extinction (see text for details). The thin solid curve represents PMS isochrones of 1×10^6 yr by Siess et al. (2000). The arrows represent the reddening vectors for 0.5 and 3.5 $M_\odot$ PMS stars, respectively. The symbols are same as in Fig. 11. The average photometric errors of the YSOs are shown in the top right corner of the diagram.

$40''$ shows that there is a gradient in free-free emission surface brightness from southeast to northwest part of the nebula. Figure 13 represents the radio continuum image of Sh 2-294 with GMRT at 1280 MHz. The radio continuum image has a resolution of $33'' \times 17''$. The map has an rms noise of $\sim$0.26 mJy beam^{-1}. The integrated flux density in the map is of $\sim$0.4 Jy, obtained by integrating down to 3 σ level, where σ is the rms noise in the map. The radio morphology shows that the thin ionization-bounded zone in southeastern direction is an indication of an IF. The decreasing intensity distribution on the opposite side signifies the region could be density bounded in northwest direction. From the optical and radio morphologies, it appears to be the flow of ionized gas in northwest direction, as expected in case of champagne model (Tenorio-Tagel 1979). Figure 14 represents the radio contours of GMRT at 1280 MHz superimposed on the K_s-band image of 2MASS in logarithmic scale. The bright source which is the possible source of ionization is located at the geometric center of the radio map and the embedded sources of region A are seen in the direction of the IF, which could be the probable young PMS sources of the Sh 2-294 region. The radio emission peaks at $\alpha = 07^h 16^m 37^s$, $\delta = -09°25'45''$. At the peak of radio emission, we did not see any significant amount of Hα emission, which could be due to presence of dense ISM/cloud that obscures the optical emission.

Assuming that Sh 2-294 is roughly spherically symmetric ionization bounded, and, neglecting absorption of ultraviolet radiation by dust inside the H II region, the measured flux density of 0.4 Jy, together with assumed distance, allow us to estimate the number of Lyman continuum photons (N_{Lyc}) emitted per second, and hence the spectral type of the exciting star. Using the relation derived by Lequeux (1980) and assuming an electron temperature of 8000 K, we estimate log $N_{\mathrm{Lyc}} = 47.90$, which corresponds to a MS spectral type earlier than B0 (Panagia 1973) and close to B0.5 (Vacca et al. 1996; Schaerer & de Koter 1997), respectively.
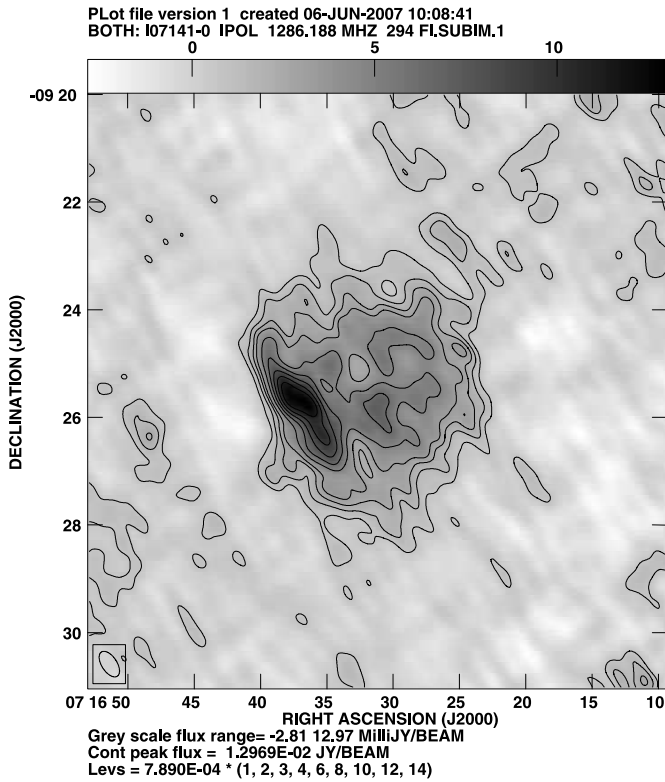
FIG. 13.—GMRT low-resolution map of the Sh 2-294 region at 1280 MHz. The resolution is $33'' \times 17''$ along P.A. $= 33.3°$. The contour levels are drawn above 3 times the rms noise of the map, which is 0.26 mJy beam^{-1}.

The differences in the spectral type is expected due to uncertainties in the effective temperature and ionizing fluxes of massive stars for a given spectral type.

5.2. Dust Continuum Emission

The strong mid- to far-infrared continuum emission detected from the local region of the interstellar cloud near region A has

FIG. 14.—2MASS K_s-band image in logarithmic scale overlaid by the GMRT radio continuum contours at 1280 MHz (blue contours). The plus sign marks the position of the exciting source of Sh 2-294. Region A is shown in the image. [See the electronic edition of the Journal for a color version of this figure.]
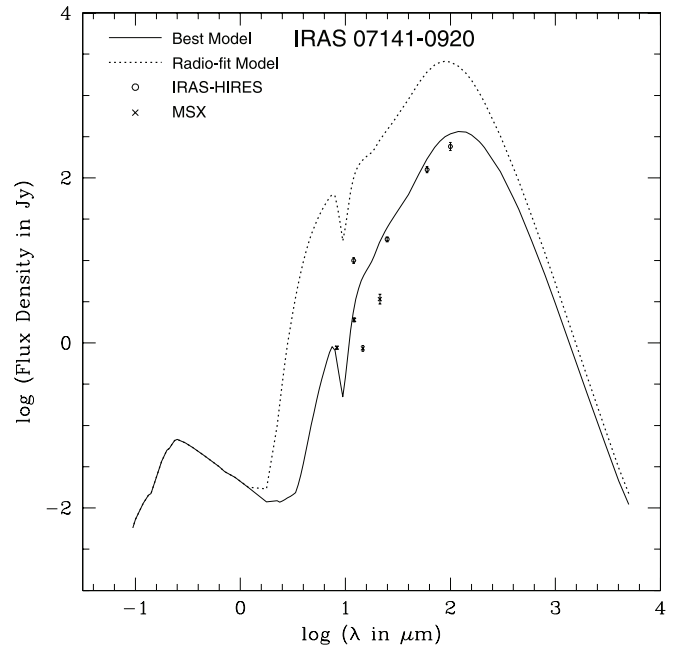

FIG. 15.—Comparison of the SED from observations and the radiative transfer models of the interstellar cloud near region A. The open circles denote IRAS HIRES data, while the crosses represent the MSX data. The HIRES fluxes are integrated over $3'$ diameter circle centered on IRAS peak. The solid curve denotes our best-fit model to the data and dashed curve represents the radio-fit model (see the text).

been modeled using a radiative transfer scheme (Mookerjea & Ghosh 1999). The energy from the central embedded source is transported through the dust and gas (only hydrogen) components of the spherical cloud and the emergent spectrum is compared with the observed SED (see Table 2). The best-fitting model is compared with the IRAS and MSX data in Figure 15 (solid curve). The far-infrared emission has been integrated over a $3'$ (diameter) region centered on IRAS 07141−0920 from the IRAS HIRES maps. There is, however, an excess emission at 12 μm, which could be due to a component of very small grains or polycyclic aromatic hydrocarbons (Degioia-Eastwood 1992). The fit is reasonably good. The parameters of this model are the r^0 density law, a radial optical depth of 5.0×10^{-2} at 100 μm, a central dust-free cavity size of 0.012 pc, and total luminosity corresponding to a ZAMS star of type B1.5. It may be noted that the predicted radio emission at 1280 MHz is too low compared to that observed locally (170 mJy within $3'$ diameter). With the aim of reproducing the observed radio emission, another model has been constructed. In order to fit the radio data well, an entirely different type of the embedded ZAMS star (O6.5) was necessary. The resulting emergent spectrum in this case is also presented for comparison in Figure 15 (dashed curve), which is at variance with the observed infrared emission. Hence, we propose that while the continuum emission from the dust component is powered by the embedded source, which might be so heavily obscured that it emits mainly in mid- to far-infrared, the ionization of the gas is maintained externally (the B0 star discussed in § 5.1).

5.3. Photodissociation Region

Figure 16 shows the continuum-subtracted $H_2(\nu) = 1−0S(1)$ 2.12 μm image smoothed with a 3×3 boxcar. The image has a field of view of $3.6' \times 3.6'$. Due to the low S/N, we can roughly describe only some of the characteristics of H_2 emission. There is a significant amount of diffuse H_2 emission seen at the center of the nebula, where the dark lane is located, which is correlated well with the CO peak. This kind of structure has been observed
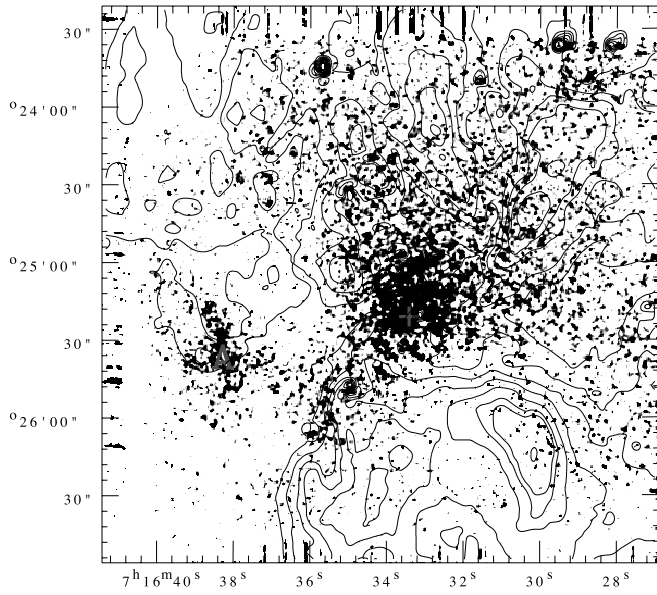
Fig. 16.—Hα continuum-subtracted contours overlaid over the continuum-subtracted H₂ (1–0)S1 line image. The prominent peaks in the contours are due to the residuals of continuum subtraction around some stars (see Fig. 17). The symbols are same as in Fig. 14. [*See the electronic edition of the Journal for a color version of this figure.*]

Fig. 17.—Contour diagram from the *MSX* A-band image (8.28 μm), overlaid on an Hα line image. The contours start at 2.1×10^6 W m^{-2} sr^{-1} and the innermost contour corresponds to a value of 2.7×10^6 W m^{-2} sr^{-1}. Residuals of the continuum subtraction around some of the stars are seen in the image. The plus sign represents the position of the central ionizing star that emits UV photons. [*See the electronic edition of the Journal for a color version of this figure.*]

in the star-forming region S255-2, where the central core of S255-2 is immersed in a region of H₂ emission with marginal evidence for limb brightening to the south (Howard et al. 1997). We also found an arc-shaped diffuse H₂ emission feature toward the east, as seen in case of Sh 2-219 (Deharveng et al. 2006) in the direction of the IF, which could be due to the interaction of massive star(s) with the nearby molecular cloud. The diffuse H₂ emission can be excited by Lyman and Werner UV photons (e.g., Chrysostomou et al. 1992) from the massive stars and thus can trace photodissociation regions (PDRs); but for a dense gas ($n_H \sim 10^6$ cm^{-3}), H₂ emission alone cannot be used to identify PDRs, and hence another PDR tracer, such as PAH emission, is necessary to trace PDRs around nebulae (Giard et al. 1994).

The far-UV radiation ($6 \leq h\nu \leq 13.6$ eV) can escape from the H II region and penetrate the surface of molecular clouds, leading to the formation of PDR in the surface layer of the clouds. PAHs within the PDR are excited by the UV photons reemitting their energy at MIR wavelengths, particularly between 6 and 10 μm. The A band (8 μm) of *MSX* includes several discrete PAH emission features (e.g., 6.6, 7.7, and 8.6 μm) in addition to the contribution from the thermal continuum component from hot dust. Figure 17 shows Hα image superimposed with *MSX* A-band contours. The 8 μm emission displays partial ring in eastern side of Sh 2-294, with diffuse emission extending toward the dark lane of optical nebula. The ring of PAH emission lies beyond the IF, indicating the interface between the ionized and molecular gas. The absence of 8 μm emission in the interior of the H II region is interpreted as the destruction of PAH molecules by intense UV radiation of the ionizing star. The peak of PAH emission matches closely with diffuse H₂ emission seen in the east. While comparing the PAH emission with Hα emission, it appears that the diffuse emission of *MSX* corresponds to dark optical features of the Hα emission.

5.4. Dust Optical Depth and Temperature Distribution

The temperature of interstellar dust is determined by a balance between radiative heating and cooling processes. Heating occurs primarily by absorption of stellar UV photons, and cooling by
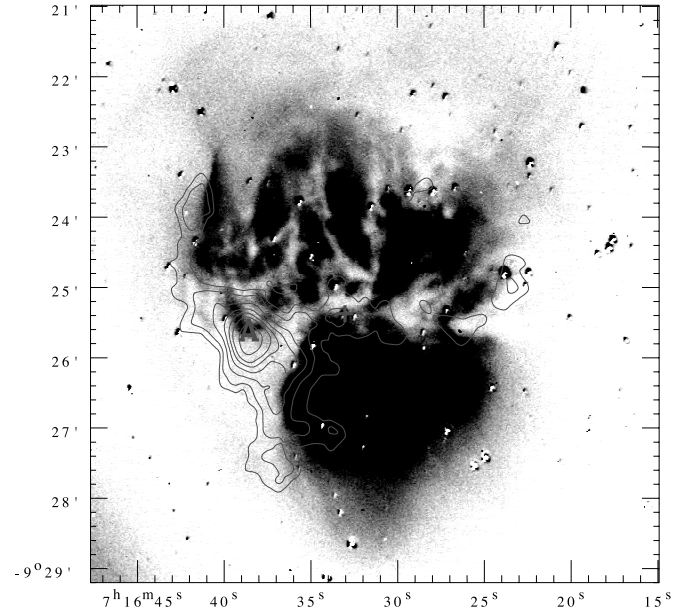
reradiation in mid- and far-infrared. A dust color temperature of each pixel using the flux ratio at 60 and 100 μm can be determined by assuming a dust emissivity law. We have used HIRES processed *IRAS* maps to generate maps of the dust color temperature [$T(60/100)$] and optical depth (τ_{25} and τ_{100}) around the Sh 2-294 region. The intensity maps at 12, 25, 60, and 100 μm were spatially averaged before computing $T(60/100)$ and (τ_{25}, τ_{100}) in a manner similar to that described by Ghosh et al. (1993) for an emissivity law of $\epsilon_\lambda \propto \lambda^{-1}$.

The HIRES processed *IRAS* maps at 12, 25, 60, and 100 μm are shown in Figure 18. The infrared emission in 60 and 100 μm maps peaks at $\alpha = 07^h16^m37^s$, $\delta = -09°25'51''$. The peak of infrared emission coincides (∼9″) with the 1280 MHz GMRT radio continuum peak and lies ∼16″ away from the peak of central density found in SSND distribution (see § 4.1) for region A. The maps at 60 and 100 μm trace the distribution of colder dust. The peak of cold dust, along with the peak of radio continuum suggest that the gas-dust coupling is rather efficient in region A, which is normally the case for regions of recent star formation. The dust emission seems to favor a southeast-to-northwest orientation, as for the cloud of the Sh 2-294 region. The extensions of the 60 and 100 μm dust emission maps have diameters larger than those of the 12 and 25 μm maps. This is due to the fact that the former has its main contribution from the cooler component of dust grains lying in the outer envelope of the cloud. Figure 19 shows the contour maps of dust optical depth at 25 and 100 μm. The τ_{100} map represents low optical depth at the position of *MSX* point source and/or region A; however, two peaks (with a peak value of $\tau_{100} \sim 0.001$) can be seen at the positions along the northeast and southwest of region A, indicating the presence of high densities in the eastern side of Sh 2-294. A gradient is seen in the optical depth map from the east to the northwest. The low optical depth in the northwest direction may be due to the lower dust column density along the path. Figure 20 presents a contour map of $T(60/100)$. The dust color temperature varies from 30 to 40 K in the map. The $T(60/100)$ and τ_{100} distributions suggest an
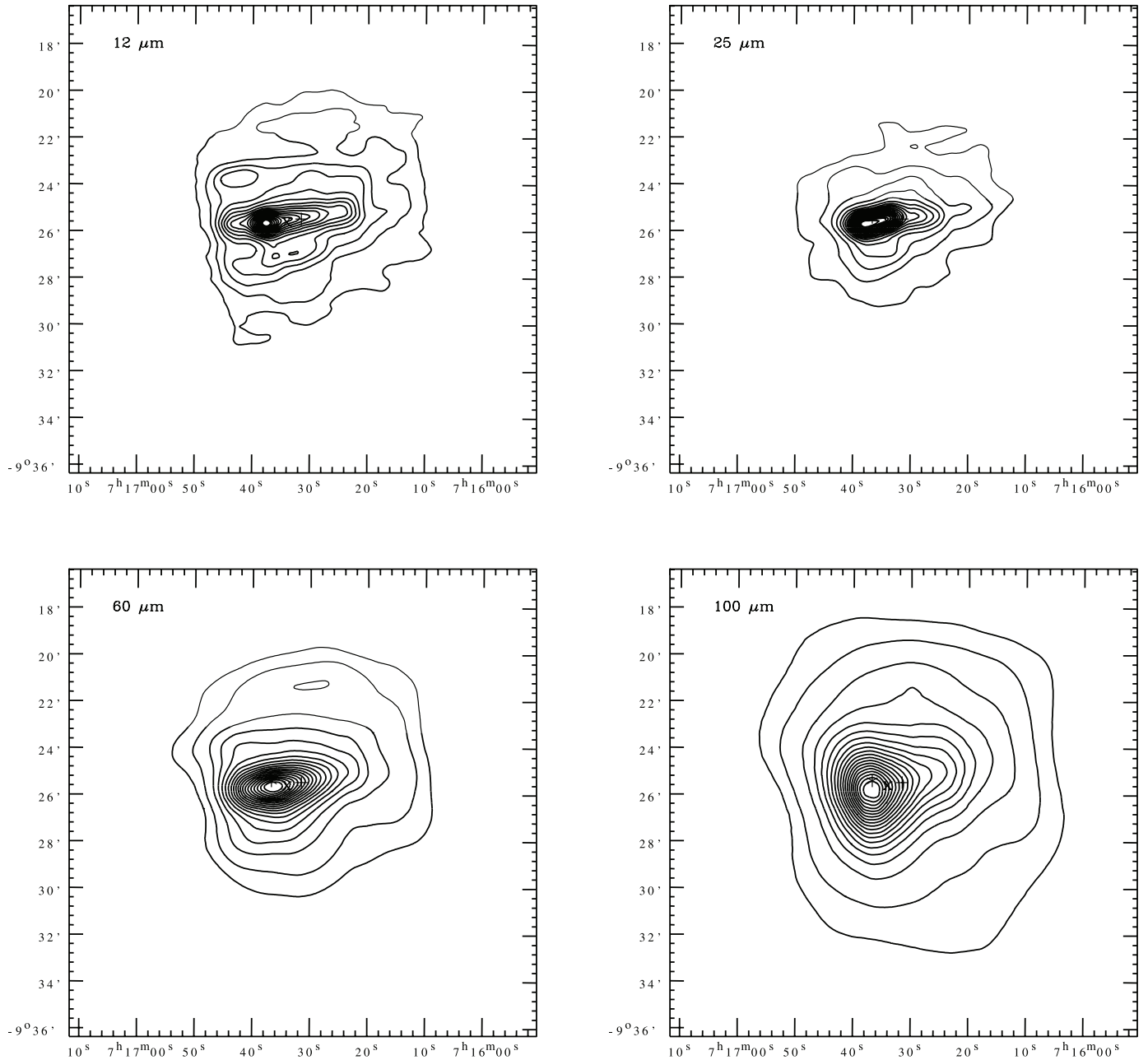
Fig. 18.—HIRES processed *IRAS* maps of the Sh 2-294 region in the four bands. *Top left*: 12 μm with peak = 41 MJy sr^{-1}. *Top right*: 25 μm with peak = 80.3 MJy sr^{-1}. *Bottom left*: 60 μm with peak = 384.2 MJy sr^{-1}. *Bottom right*: 100 μm with peak = 600.5 MJy sr^{-1}. The isophot contour levels in 12 and 25 μm are 95, 90, 80, 70, 60, 50, 40, 30, 20, 10, and 5 percent, and in 60 and 100 μm are 95, 90, 80, 70, 60, 50, 40, 30, 20, 10, 5, and 2.5 percent of the respective peaks. The abscissa and the ordinates are in J2000.0 epoch. The symbols are same as in Fig. 3.

anticorrelation, such as the peak position of τ_{100} map corresponds to a low color temperature of $\sim$31 K. The relatively high temperature around region A may be due to the radiation from young stars of the region. The cometary morphology of the map could be due to inhomogeneous distribution of dust in Sh 2-294.

6. STAR FORMATION SCENARIO AROUND Sh 2-294

6.1. *Spatial Distribution of Young Sources*

Figure 21 shows the continuum-subtracted molecular hydrogen 2.12 μm image of field of view 3.6′ × 3.6′, overlaid by the GMRT radio continuum contours (*blue color*). The red contours represent the *MSX* 8 μm emission, which are generally attributed to PAHs. The spatial distribution of Class II, Class I, probable

Herbig Ae/Be sources, and sources detected only in H and K_s bands are shown in different symbols. The symbols for the sources are same as in ($H - K$) versus K CMD (Fig. 11). We also find that there are five sources detected only in the K_s band, but not in H and J bands. These sources may also be probable YSO candidates; we represented them by red filled circles in Figure 21. We found a nonuniform distribution of young sources in the Sh 2-294 star-forming region. The complex seems to be composed of sources of different evolutionary stages aligned from northwest to southeast along the dark lane seen in Hα image (see Fig. 1). They are mainly concentrated around the region where diffuse H$_2$ emission is seen. Most of the Herbig Ae/Be and Class II sources are seen in the northwest, but in contrast, sources detected in H and K_s bands and only in K_s band are seen toward the
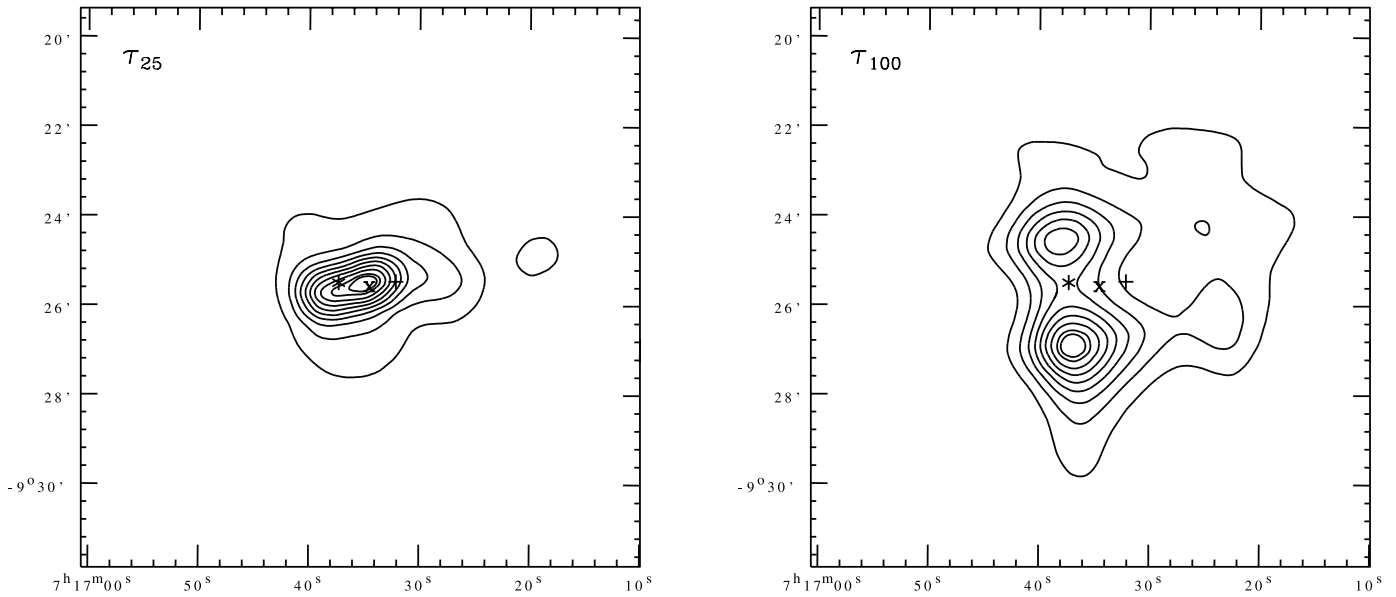
Fig. 19.—*Left*: The dust optical depth (τ_{25}) distribution from the HIRES 12 and 25 μm maps for the region around Sh 2-294, assuming a dust emissivity law of $\epsilon_\lambda \propto \lambda^{-1}$. The contours represent 95, 90, 80, 70, 60, 50, 40, 30, 20, and 10 percent of the global peak value of 7.9×10^{-7}. *Right*: The dust optical depth (τ_{100}) distribution from the HIRES 60 and 100 μm maps for the region around Sh 2-294, assuming a dust emissivity law of $\epsilon_\lambda \propto \lambda^{-1}$. The contours represent 95, 90, 80, 70, 60, 50, 40, 30, 20, and 10 percent of the global peak value of 1.2×10^{-3}. The symbols are same as in Fig. 3.

southeast. The spatial distribution suggests that the southeastern region is less evolved than other parts of the Sh 2-294 star-forming region. The regions (northeast and southwest), which are most probably ionized by a massive star located at the center of the nebula, have lack of Class II, Class I, and other probable YSOs, which implies that star formation activity has subsided in these directions due to intense UV photons. We identified a source from *MSX* PSC at $\alpha = 07^h16^m38^s$, $\delta = -09°25'40''$ that coincides with the peak by found SSND distribution for region A. In the Sh 2-294 region, the young sources in and around region A are observed in PDR region along the direction of the IF. The morphology of the PDR and H$_2$ emission in comparison with radio continuum emission gives evidence of interaction of massive star(s) with the nearby cloud. The close association of the partially

embedded cluster (region A) adjacent to the H II region in the direction of the IF therefore suggests that the star formation at the border of Sh 2-294 may be due to expansion of H II region. It is therefore necessary to invoke the classical triggering scenario of Elmegreen & Lada (1977), in which UV radiation compresses the abundant nearby gas, leading to the star formation.

6.2. *Age of the Ionizing Source and the* H II *Region*

The spectral type of ionizing star is of B0 $\pm$ 0.5 V (see § 4.3), which agrees well with the spectral type derived from radio continuum emission at 1280 MHz and also from NIR CC diagram.
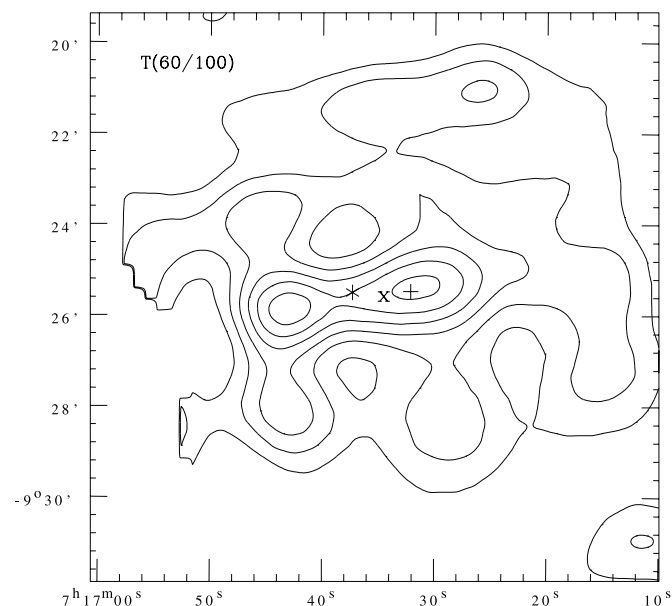

Fig. 20.— Dust color temperature [$T(60/100)$] distribution. The contours correspond to the temperatures from 30 to 40 K in steps of 2 K. The abscissa and the ordinates are in J2000.0 epoch. The symbols are same as in Fig. 3.
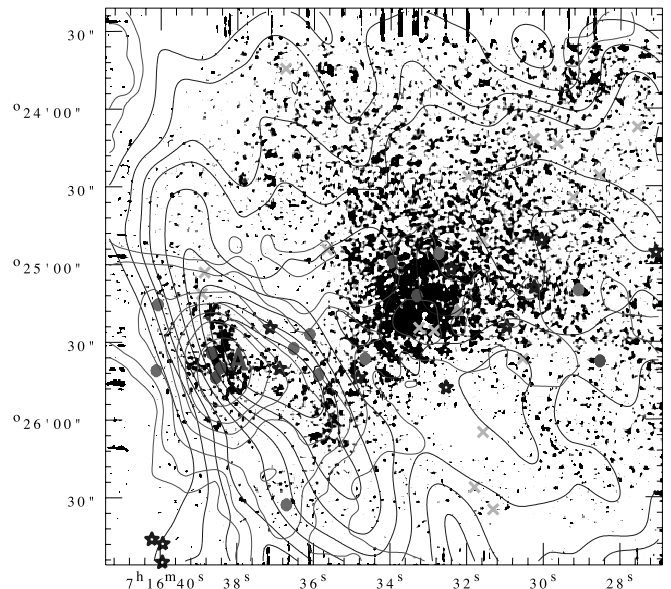

Fig. 21.—Continuum-subtracted molecular hydrogen 2.12 μm line image from HCT overlaid by the GMRT radio continuum contours (*blue*). The red contours represent the distribution of warm dust from *MSX* A band (8.28 μm). Spatial distributions of Class II (*stars*), Class I (*filled triangles*), probable Herbig Ae/Be sources (*crosses*), sources detected only in H and K_s bands (*filled magenta circles*), and sources detected only in K_s band (*filled red circles*) are shown in the figure. [*See the electronic edition of the Journal for a color version of this figure.*]

Therefore, we assume the spectral type of the massive star of B0 V for further discussion. The probable age ($\sim4\times10^6$ yr) of ionizing star compared to the MS life time of B0 type star ($\sim1\times10^7$ yr), implies that the H II region is still under expansion. The dynamical age of Sh 2-294 can be estimated by using the model by Dyson & Williams (1997), assuming ionized gas of pure hydrogen at constant temperature in an uniform medium of constant density. If the H II region associated with Sh 2-294 is excited by a B0 V star, which emits $\sim78.75\times10^{46}$ (log $N_{Lyc}\sim47.90$) ionizing photons per second and is expanding into a homogeneous medium of density 10^3 (10^2) cm^{-3}, will form a Strömgren radius (r_s) of ~0.17 (0.79) pc. The initial phase is overpressured compared to the neutral gas and will expand into the medium of radius r_i at time t as

$$r_i = r_s\left(1 + \frac{7C_{II}t}{4r_s}\right)^{4/7},\qquad(4)$$

The observed diameter of the ionized gas from GMRT radio contour is $\sim4.7'$, which corresponds to a physical diameter of about 6.6 pc at a distance of 4.8 kpc. An assumed sound speed (C_{II}) of 11.4 (4.0) km s^{-1} in the ionized gas of density 10^3 cm^{-3} yields dynamical age of $\sim1.5(4.2)\times10^6$ yr, whereas in the lower density medium (for example 10^2 cm^{-3}) the above velocity range will yield $\sim0.4(1.2)\times10^6$ yr. However, the uncertainty in age estimation cannot be ignored because of the assumption of a uniform medium and because the velocity of expansion changes with time. One would then expect an expanding IF to be preceded by a swept-up shell of cool neutral gas as it erodes into a neutral cloud. We have detected a half-ring of *MSX* dust emission toward the eastern part of H II region, which is an indication that neutral gas surrounds the ionized gas.

6.3. *Triggered Star Formation*

Triggered star formation is a sequential process in which star formation at the interface between H II regions and molecular clouds can be triggered by the ionization or shock fronts produced by massive stars. The mechanisms mainly responsible for triggered star formation have been discussed, such as the "radiation-driven implosion" (RDI) and "collect-and-collapse" models. In the RDI model, the expanding ionization front compresses the preexisting molecular clumps, leading to density enhancements, which, when it exceeds the local critical mass, collapses to form new stars (Lefloch & Lazareff 1994; Gorti & Hollenbach 2002). In the collect-and-collapse model, the neutral material accumulates between the ionization front of the H II region and the shock front in the neutral gas. This compressed, shocked material may be dynamically unstable on a short internal-crossing timescale, leading to the formation of cometary globules and bright rims (Garcia-Segura & Franco 1996) or the compressed layer may become gravitationally unstable along its surface, on a long timescale (Elmegreen & Lada 1977; Zavagno et al. 2006), leading to the formation of massive fragments forming massive stars and/or clusters.

The CMDs (Fig. 8) indicate that the ionizing source may have a maximum age of $\sim4\times10^6$ yr. It is rather difficult to estimate the age of the cluster associated with region A as it has no optical counterpart and has poor statistics; however, the age of region A can be assigned on the basis of the age of CTT stars. The life time of CTTs ranges from a few times 10^5 to few times 10^6 yr. Region A contains two CTT stars, and their positions in intrinsic ($J - H$) versus J CMD suggest an age of $<1\times10^6$ yr. However, this age should be considered as an approximate estimation because of the

uncertainty in determination of extinction as well as error in colors. On the basis of the fraction of NIR excess stars (see § 4.6.1), an age of $\sim1\times10^6$ yr can also be assigned to region A. If we assume that the distance between the ionizing star and the young stars in region A is closed to a projected distance of ~1.8 pc (1.3') and that the ionization front expands at a sound speed of 4.0 (11.4) km s^{-1}, it would take approximately $4.6(1.7)\times10^5$ yr to reach the surface of the cloud and can induce second generation stars at the border. The protostellar phase in the clouds last for $\sim10^5$ yr. Therefore, the age difference between the young sources in region A and central ionizing source, keeping in mind the uncertainty in assigning the ages to the clusters, seems to be consistent with the hypothesis that star formation at the border may be due to RDI process.

However, the possibility of "collect-and-collapse" process cannot also be ruled out by considering the following evidence. The radio observation reveals that Sh 2-294 is a roughly spherically ionized region and is surrounded by half-ring of *MSX* dust emission in the mid-IR (see Fig. 17). The ring is enhanced in the middle of the arc of dust emission. We found a *MSX* point source at the center of dust peak. The presence of dust ring beyond the IF indicates that the neutral gas surrounds the H II region. An embedded cluster (region A) is associated with the dust ring within 2MASS detection limit and its central density lies close to the position of *MSX* point source, satisfying most of the predictions proposed by the Deharveng et al. (2005) for star formation to occur at the border due to collect-and-collapse model. For example the morphology of the Sh 2-294 region is almost similar to the selected H II candidates by Deharveng et al. (2005), which are likely to be examples of star formation at the border by this process. However, to look for the distribution of dense fragments around Sh 2-294, as seen in case of RCW 79 (Zavagno et al. 2006), one needs millimeter observations. The fact that the dynamical age of H II region is of $\sim1.5\times10^6$ yr, comparable to the age of the stars associated with the region A and the presence of a ZAMS B1.5 star, further supports the formation of massive star following the collapse of thin shell of neutral matter, as predicted by collect-and-collapse model.

With the existing observations and data, it will be early to establish or rule out either of the scenarios. To provide a conclusive answer to the above mentioned star formation scenarios in Sh 2-294, we need deep optical, NIR, and CO observations, as well as millimeter observations.

7. SUMMARY

In this paper we provide the first global view of star formation around the Sh 2-294 region. Our multiwavelength data provides a detailed insight into distribution and nature of the young stellar objects, as well as into the morphology of the thermal ionized gas and dust emissions. Based on the 2MASS data, we identify a star cluster at the center of Sh 2-294 and a distinct group of reddened stars (small cluster) located at 1.8 pc to the east of Sh 2-294. The optical and near-infrared color-color and color-magnitude diagrams have been constructed to estimate the ratio of the total to the selective extinction, reddening, distance, and spectral types of young stellar objects. The narrowband imaging in Hα and the radio continuum map based on GMRT observation at 1280 MHz have been used to trace the ionized gas, which show interesting morphological details, including an arc-shaped structure in southeast direction and creation of lower density zones in the northwest direction through which the ionized gas can escape. We identified the most luminous member of the cluster situated at the center of the ionized gas and derived its spectral type which is consistent with an $\sim$B0 main-sequence star. The number of Lyman

continuum photons from the radio flux suggests that this single star is responsible for the ionization of the nebula. The PDR at the interface between the ionized gas and the molecular cloud is traced to the southeast direction by a half-ring of the PAH feature in *MSX* and diffuse H_2 emission. The morphological correlation between ionized gas, PDR, and H_2 emission leads us to conclude that there is a high degree of interaction of UV photons from B0 star with the nearby molecular cloud in northeastern direction. The small cluster is found at the peak of the dust ring. The spatial distribution of the YSOs (Class II sources, sources detected in H and K_s bands and those detected only in K_s band) indicates that the region around a small cluster is less evolved and suggests that the star formation activity observed at the border of the Sh 2-294 region is possibly triggered by the expansion of H II region.

REFERENCES

Aumann, H. H., Fowler, J. W., & Melnyk, M. 1990, AJ, 99, 1674
Baba, D., et al. 2004, ApJ, 614, 818
Bertelli, G., Bressan, A., Chiosi, C., & Fagotta, F. 1994, A&AS, 106, 275
Bessell, M., & Brett, J. M. 1988, PASP, 100, 1134
Bica, E., Dutra, C. M., & Barbuy, B. 2003, A&A, 397, 177
Blair, G. N., Peters, W. L., Vanden Bout, P. A. 1975, ApJ, 200, L161
Blitz, L., Fich, M., & Stark, A. A. 1982, ApJS, 49, 183
Carpenter, J. M. 2001, AJ, 121, 2851
Chini, R., & Wargau, W. H. 1990, A&A, 227, 213
Chrysostomou, A., Brand, P. W. J. L., Burton, M. G., & Moorhouse, A. 1992, MNRAS, 256, 528
Cohen, J. G., Persson, S. E., Elias, J. H., & Frogel, J. A. 1981, ApJ, 249, 481
Cutri, R. M., et al. 2003, 2MASS All-Sky Catalog of Point Sources (Pasadena: NASA/IPAC), http://irsa.ipac.caltech.edu/applications/Gator
Deharveng, L., Lefloch, B., Massi, F., Brand, J., Kurtz, S., Zavagno, A., & Caplan, J. 2006, A&A, 458, 191
Deharveng, L., Zavagno, A., & Caplan, J. 2005, A&A, 433, 565
Degioia-Eastwood, K. 1992, ApJ, 397, 542
Dyson, J. E., & Williams, D. A. 1997, The Physics of the Interstellar Medium (2nd ed.; Bristol: IOP)
Egan, M. P., et al. 2003, *MSX*6C Infrared Point Source Catalog (AFRL-VS-TR-2003-1589; Bedford: AFCRL)
Elmegreen, B. G., & Lada, C. J. 1977, ApJ, 214, 725
Felli, M., & Churchwell, E. 1972, A&AS, 5, 369
Felli, M., & Harten, R. H. 1981, A&A, 100, 28
Felli, M., Harten, R. H., Habing, H. J., & Israel, F. P. 1978, A&AS, 32, 423
Fich, M. 1993, ApJS, 86, 475
Forte, J. C. 1978, AJ, 83, 1199
Garcia-Segura, G., & Franco, J. 1996, ApJ, 469, 171
Ghosh, S. K., Verma, R. P., Rengarajan, T. N., Das, B., & Saraiya, H. T. 1993, ApJS, 86, 401
Giard, M., Bernard, J. P., Lacombe, F., Normand, P., & Rouan, D. 1994, A&A, 291, 239
Gomez, M., Hartmann, L., Kenyon, S. J., & Hewett, R. 1993, AJ, 105, 1927
Gorti, U., & Hollenbach, D. 2002, ApJ, 573, 215
Haisch, K. E., Lada, E. A., & Lada, C. J. 2000, AJ, 120, 1396
———. 2001, AJ, 121, 2065
He, L., Whittet, D. C. B., Kilkenny, D., & Spencer Jones, J. H. 1995, ApJS, 101, 335
Henkel, C., Guesten, R., & Haschick, A. D. 1986, A&A, 165, 197
Hillenbrand, L. A., Strom, S. E., Vrba, F. J., & Keene, J. 1992, ApJ, 397, 613
Horner, D. J., Lada, E. A., & Lada, C. J. 1997, AJ, 113, 1788
Howard, E. M., Pipher, J. L., & Forrest, W. 1997, ApJ, 481, 327
Jacoby, G. H., Hunter, D. A., & Christian, C. A. 1984, ApJS, 56, 257
Johnson, H. L. 1966, ARA&A, 4, 193
Kenyon, S. J., & Hartmann, L. 1995, ApJS, 101, 117
Koornneef, J. 1983, A&A, 128, 84
Lada, C. J., & Adams, F. C. 1992, ApJ, 393, 278

Lada, C. J., et al. 2000, AJ, 120, 3162
Landolt, A. U. 1992, AJ, 104, 340
Lefloch, B., & Lazareff, B. 1994, A&A, 289, 559
Lequeux, J. 1980, Star Formation, ed. A.Maeder & L. Martinet (Sauverny: Geneva Obs.), 77
Mateo, M., & Hodge, P. 1986, ApJS, 60, 893
Mathis, J. S. 1990, ARA&A, 28, 37
Meyer, M. R., Calvet, N., & Hillenbrand, L. A. 1997, AJ, 114, 288
Moffat, A. F. J., Jackson, P. D., & Fitzgerald, M. P. 1979, A&AS, 38, 197
Mookerjea, B., & Ghosh, S. K. 1999, J. Astrophys. Astron., 20, 1
Neckel, T., & Chini, R. 1981, A&AS, 45, 451
Ojha, D. K., Ghosh, S. K., Kulkarni, V. K., Testi, L., Verma, R. P., & Vig, S. 2004a, A&A, 415, 1039
Ojha, D. K., et al. 2004b, ApJ, 608, 797
———. 2004c, ApJ, 616, 1042
Panagia, N. 1973, AJ, 78, 929
Pandey, A. K., Ogura, K., & Sekiguchi, K. 2000, PASJ, 52, 847
Pandey, A. K., Upadhyay, K., Nakada, Y., & Ogura, K. 2003, A&A, 397, 191
Price, S. D., Egan, M. P., Carey, S. J., Mizuno, D. R., & Kuchar, T. A. 2001, AJ, 121, 2819
Schaerer, D., & de Koter, A. 1997, A&A, 322, 598
Schmidt-Kaler, Th. 1982, in Stars and Star CLusters, ed. K Schaifers & HH. Voight (Berlin: Springer), 19
Siess, L., Dufour, E., & Forestini, M. 2000, A&A, 358, 593
Silverman, B. W. 1986, Density Estimation for Statistics and Data Analysis (London: Chapman & Hall)
Sharpless, S. 1959, ApJS, 4, 257
Sugitani, K., et al. 2002, ApJ, 565, L25
Swarup, G., Ananthakrishnan, S., Kapahi, V. K., Rao, A. P., Subrahmanya, C. R., & Kulkarni, V. K. 1991, Curr. Sci., 60, 95
Tapia, M., Roth, M., Costero, R., Echevarria, J., & Roth, M. 1991, MNRAS, 253, 649
Teixeira, P. S., Fernandes, S. R., Alves, J. F., Correia, J. C., Santos, F. D., Lada, E. A., & Lada, C. J. 2004, A&A, 413, L1
Tej, A., Ojha, D. K., Ghosh, S. K., Kulkarni, V. K., Verma, R. P., Vig, S., & Prabhu, T. P. 2006, A&A, 452, 203
Tenorio-Tagle, G. 1979, A&A, 71, 59
The, P. S., & Groot, M. 1983, A&A, 125, 75
Vacca, W. D., Garmany, C. D., & Shull, J. M. 1996, ApJ, 460, 914
Walborn, N. R., & Fitzpatrick, E. L. 1990, PASP, 102, 379
Walker, A. R. 1985, MNRAS, 213, 889
Wegner, W. 1993, Acta Astron., 43, 209
Whittet, D. C. B., van Breda, I. G., & Glass, I. S. 1976, MNRAS, 177, 625
Winkler, H. 1997, MNRAS, 287, 481
Wouterloot, J. G. A., & Brand, J. 1989, A&AS, 80, 149
Zavagno, A., Deharveng, L., Comeron, F., Brand, J., Massi, F., Caplan, J., L., & Russeil, D. 2006, A&A, 446, 171